minerals

MDPI

Article

Provenance of Wushan Loess in the Yangtze Three Gorges Region: Insights from Detrital Zircon U-Pb Geochronology and Late Pleistocene East Asian Monsoon Variations

Xulong Hu [1], Yufen Zhang [1,*], Chang'an Li [2,*], Guoqing Li [1], Juxiang Liu [3], Yawei Li [4], Jianchao Su [5] and Mingming Jia [6]

[1] Hubei Subsurface Multi-Scale Imaging Key Laboratory, School of Geophysics and Geomatics, China University of Geosciences, Wuhan 430074, China; huxulong@cug.edu.cn (X.H.); lgq123@cug.edu.cn (G.L.)
[2] School of Geography and Information Engineering, China University of Geosciences, Wuhan 430074, China
[3] School of Computer and Information Science, Hubei Engineering University, Xiaogan 432000, China; liujuxiang1225@hotmail.com
[4] College of Tourism and Planning, Pingdingshan University, Pingdingshan 467400, China; liyaweicug@163.com
[5] Yellow River Engineering Consulting Co., Ltd., Zhengzhou 450003, China; alan1cug@163.com
[6] Institute of Geography, Henan Academy of Sciences, Zhengzhou 450046, China; jmm19912022@163.com
* Correspondence: zhyfcug@163.com (Y.Z.); chanli@cug.edu.cn (C.L.)

Abstract

The Wushan Loess, situated in the Yangtze Three Gorges region of China, represents the southernmost aeolian loess deposit in China and provides critical insights into Late Pleistocene paleoenvironmental conditions and East Asian monsoon dynamics. Despite its significance, the genesis and provenance of this unique loess deposit remain controversial. This study employs an integrated multi-proxy approach combining detrital zircon U-Pb geochronology, optically stimulated luminescence (OSL) dating, and detailed grain size analysis to systematically investigate the provenance and depositional mechanisms of the Wushan Loess. Three representative loess–paleosol profiles (Gaotang-GT, Badong-BD, and Zigui-ZG) were analyzed, yielding 17 OSL ages, 729 grain size measurements, and approximately 420 analyses per profile were conducted, yielding 1189 valid ages (GT 406, BD 391, ZG 402). OSL chronology constrains the deposition period to 18–103 ka (Marine Isotope Stages 2–5), coinciding with enhanced East Asian winter monsoon activity during the Last Glacial period. Grain size analysis reveals a dominant silt fraction (modal size: 20–25 μm) characteristic of aeolian transport, with coarse silt (20–63 μm) averaging 47.1% and fine silt (<20 μm) averaging 44.2% of the sediments. Detrital zircon U-Pb age spectra exhibit consistent major peaks at 200–220 Ma, 450–500 Ma, 720–780 Ma, and 1800–1850 Ma across all profiles. Kernel Density Estimation (KDE) and Multi-Dimensional Scaling (MDS) analyses indicate a mixed provenance model. Non-negative least squares (NNLS) unmixing confirms this quantitative source apportionment., dominated by proximal contributions from the upper Yangtze River basin (including the Three Gorges area and Sichuan Basin, ~65%–70%), supplemented by distal dust input from the Loess Plateau and northern Chinese deserts (~30%–35%). This study establishes for the first time a proximal-dominated provenance model for the Wushan Loess, providing new evidence for understanding southern Chinese loess formation mechanisms and Late Pleistocene East Asian monsoon evolution.

Keywords: Wushan Loess; provenance tracing; detrital zircon U-Pb dating; optically stimulated luminescence (OSL) dating; grain size characteristics; aeolian deposition; East Asian monsoon

check for updates

Academic Editor: Juan Manuel Martín-García

Received: 13 October 2025
Revised: 5 November 2025
Accepted: 7 November 2025
Published: 9 November 2025

Citation: Hu, X.; Zhang, Y.; Li, C.; Li, G.; Liu, J.; Li, Y.; Su, J.; Jia, M. Provenance of Wushan Loess in the Yangtze Three Gorges Region: Insights from Detrital Zircon U-Pb Geochronology and Late Pleistocene East Asian Monsoon Variations. *Minerals* **2025**, *15*, 1180. https://doi.org/10.3390/min15111180

Copyright: © 2025 by the authors. Licensee MDPI, Basel, Switzerland. This article is an open access article distributed under the terms and conditions of the Creative Commons Attribution (CC BY) license (https://creativecommons.org/licenses/by/4.0/).

1. Introduction

Loess deposits serve as sensitive indicators of inland aridification in Asia, recording dust transport patterns and climatic evolution over geological timescales [1]. The Chinese loess deposits are extensively distributed, has provided invaluable paleoclimatic records spanning the past ~22 million years [2,3]. Recent studies using large-number detrital zircon U-Pb geochronology have revealed that global cooling was responsible for the formation of the Chinese Loess Plateau during the Late Miocene [4], highlighting the critical role of climate-tectonic interactions in loess formation.

The Wushan Loess, located in the Yangtze Three Gorges region, represents the southernmost extent of Chinese loess distribution and occupies a critical position along the transport pathway between the primary northern dust sources (Loess Plateau, Gobi deserts) and the humid regions of southern China (middle and lower Yangtze River basin) [5]. Its provenance and formation mechanisms are directly linked to the north–south expansion of the East Asian monsoon system, making it a key archive for understanding Late Pleistocene atmospheric circulation patterns [6,7].

Detrital zircon U-Pb geochronology has emerged as a powerful tool for provenance analysis, as zircon is a highly stable mineral characterized by durability, stable physical and chemical attributes, low common Pb concentration, and enrichment in U and Th [8,9]. Recent advances have demonstrated the effectiveness of large-n detrital zircon datasets (typically > 300 grains) in discriminating sediment sources and reconstructing transport pathways in various depositional environments [10,11]. Single grain zircon U-Pb geochronology has demonstrated great potential in extracting tectonic and atmospheric circulation signals carried by aeolian, fluvial, and fluviolacustrine sediments [12,13]. Recent provenance studies of Chinese loess using detrital zircon U-Pb dating have successfully traced dust sources from the Loess Plateau [14], revealed the genetic linkage between the Yellow River and northern deserts [15], and documented provenance variations in response to climate change [16,17]. When combined with optically stimulated luminescence (OSL) dating for chronological constraints and grain size analysis for transport mechanism interpretation, this multi-proxy approach provides comprehensive insights into loess formation processes [18,19].

Several previous detrital zircon U-Pb studies have provided valuable provenance constraints for potential source regions of the Wushan Loess. In the Loess Plateau region, Bird et al. [2015] [10] conducted comprehensive U-Pb analyses revealing temporal variations in dust sources across the Quaternary, identifying contributions from the Gobi deserts, Qaidam Basin, and northern sandy lands [14]. Stevens et al. [2013] [10] established the genetic linkage between the Yellow River, Mu Us Desert, and the Chinese Loess Plateau through combined zircon U-Pb and heavy mineral analysis, demonstrating that the Yellow River serves as both a source and pathway for loess material [15]. For the upper Yangtze River basin, recent studies have characterized the detrital zircon age spectra of modern river sediments, revealing dominant age populations at 200–300 Ma (Indosinian orogeny), 400–500 Ma (Caledonian orogeny), and 700–900 Ma (Neoproterozoic) that reflect the geological evolution of the Yangtze Craton and surrounding orogenic belts [20,21]. In the Sichuan Basin, detrital zircon studies of Cenozoic sediments have documented provenance changes related to Tibetan Plateau uplift and drainage reorganization [22,23]. Studies of northern Chinese deserts (Tengger, Badain Jaran, Mu Us, Otindag, and Horqin) have characterized their distinctive zircon age signatures, with the Tengger and Mu Us deserts showing ages of 200–500 Ma and 1800–2000 Ma, while the Otindag and Horqin sandy lands display broader age distributions including significant Paleozoic and Precambrian components [24,25]. These compiled datasets provide essential comparative frameworks for identifying the sources of the Wushan Loess, though direct application to southern

Chinese loess deposits has been limited by the lack of systematic multi-profile studies in transitional monsoon boundary zones.

Despite previous investigations focusing on stratigraphic and chronological aspects of the Wushan Loess [13,14], significant controversies persist regarding (1) the specific sediment sources (upper Yangtze River basin vs. northern deserts), (2) transport mechanisms (aeolian vs. fluvial), and (3) the relative contributions of proximal and distal sources. Previous studies on Chinese loess have shown that southern loess deposits, such as the Xiashu Loess [13–15] in the lower Yangtze River reaches, have mixed sources of proximal materials and distal dust from arid areas of North China [15], but the specific provenance signature of the Wushan Loess remains unresolved.

The complex topography of the Wushan region, characterized by deep river valleys and mountainous terrain, creates unique depositional environments that may influence both the preservation of loess sequences and the interpretation of provenance signals [16,17]. Previous studies on Wushan Loess provenance have been limited by single-profile analyses [26,27], reliance on single proxy approaches [28], small detrital zircon sample sizes (<100 grains) [29], and the lack of quantitative provenance tracing methods [30,31], which may not capture the full complexity of mixed source signatures characteristic of loess deposits in monsoon transitional zones [32,33]. Furthermore, earlier studies primarily employed qualitative visual comparison of age spectra rather than robust statistical approaches such as multi-dimensional scaling (MDS) or unmixing models that can quantitatively apportion source contributions [34,35].

This study addresses these limitations through a comprehensive multi-profile, multi-proxy investigation of three spatially distinct Wushan Loess profiles (Gaotang, Badong, and Zigui). We employ high-precision detrital zircon U-Pb geochronology with large datasets (420 zircons per profile), OSL chronology, and detailed grain size analysis to: (1) establish a robust chronological framework for Wushan Loess deposition, (2) identify the material sources and quantify their relative contributions, (3) elucidate the depositional processes and transport mechanisms, and (4) provide new insights into Late Pleistocene aeolian dynamics and East Asian monsoon evolution in the upper-middle Yangtze River region.

2. Geological Setting

The Three Gorges region serves as a critical transitional zone between the Sichuan Basin to the west and the Jianghan Basin to the east, featuring complex topography with elevations ranging from 170 to 1500 m [20,21]. This area encompasses diverse geomorphological features, including steep slopes, deep valleys, and karst landscapes, which profoundly influence sediment deposition and preservation patterns [22] (Figure 1a).

Consequently, the Wushan Loess exhibits a patchy spatial distribution, primarily shaped by canyon topography and subsequent hillslope geomorphic processes, resulting in significant variations in thickness and integrity across different landform positions [23–25]. The typical stratigraphic structure of the Wushan Loess can be divided into four loess layers ($L_{1\text{-}1}$, $L_{1\text{-}3}$, $L_{1\text{-}5}$, L_2), two weakly developed paleosol layers (manifesting as calcareous nodules, corresponding to $L_{1\text{-}2}$ and $L_{1\text{-}4}$), and one fully developed paleosol layer (S_1) (Figure 1b–g)., which is comparable to the upper Malan Loess and Lishi Loess (L_1–L_2) on the Loess Plateau. This stratigraphic sequence indicates a formation period spanning from the Late Pleistocene to the present, approximately 100,000 years ago, recording climatic and environmental changes since the Last Glacial Maximum.

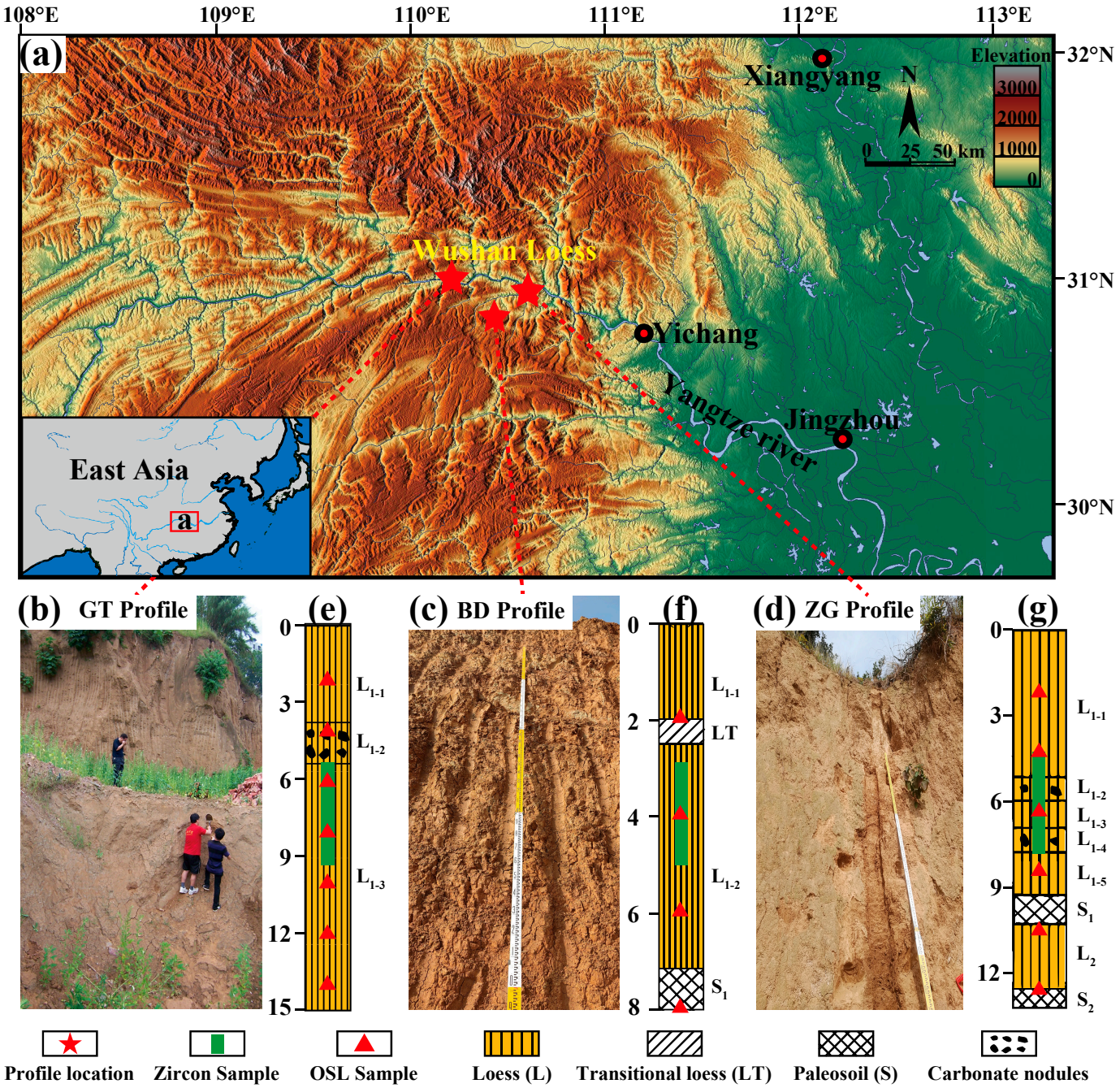


Figure 1. Study area and sampling points. (**a**) Geographic location of the Wushan Loess deposits in the Three Gorges region of the upper Yangtze River basin, East Asia. (**b**–**d**) Field Photo of profiles at Gaotang (GT), Badong (BD), and Zigui (ZG) sites. (**e**–**g**) Stratigraphic logs of the representative loess-paleosol profiles, illustrating depositional units and sampling depths.

In comparison to northern loess deposits, the Wushan Loess displays distinctive geochemical characteristics: its loess layers are darker and slightly reddish, while the S_1 paleosol layer features evident ferromanganese films on fracture surfaces, signifying stronger pedogenic processes than those in northern loess [26,27]. These differences arise primarily from its geographical proximity to the East Asian summer monsoon domain, fostering a warmer and more humid climate. The sedimentary sequence of the Wushan Loess not only provides high-resolution paleoenvironmental records but also offers crucial evidence for understanding the evolution of the East Asian monsoon system. Notably, due to the complex topography of the Three Gorges region, the Wushan Loess exhibits varying

depositional features at different elevations, potentially reflecting distinct sedimentary processes and proportional contributions from various sources.

To capture the spatial variability and overall characteristics of the Wushan Loess, three complete profiles were selected, spanning elevations from 169 to 1026 m, diverse geomorphological positions (e.g., high terraces and gentle slopes), and distances from the Yangtze River ranging from 0 to 30 km. These profiles, located approximately 60 km apart, comprise: Gaotang Street in Wushan County (GT, 31.08° N, 109.88° E, 169 m a.s.l.), Yesanguan Town in Badong County (BD, 30.63° N, 110.33° E, 1026 m a.s.l.), and Shazhenxi Town in Zigui County (ZG, 30.99° N, 110.62° E, 192 m a.s.l.) (Figure 1b–d).

3. Sampling and Methods

3.1. Sample Collection and Stratigraphy

Three loess-paleosol profiles were systematically sampled in the Wushan region: GT (~15 m thick), BD (~8 m thick), and ZG (~13 m thick). The GT profile contains three loess units ($L_{1\text{-}1}$ to $L_{1\text{-}3}$), with $L_{1\text{-}2}$ containing carbonate nodules (Figure 1b,e). The BD profile includes $L_{1\text{-}1}$, a transitional loess layer (LT), $L_{1\text{-}2}$, and a basal paleosol layer (S_1) (Figure 1c,f). The ZG profile comprises five loess units ($L_{1\text{-}1}$ to $L_{1\text{-}5}$), two paleosol layers (S_1 and S_2), and an intermediate loess layer (L_2), with carbonate nodules present in $L_{1\text{-}2}$ and $L_{1\text{-}4}$ (Figure 1d,g).

Sample collection followed established protocols for multi-proxy analysis. OSL samples were collected at ~2 m intervals from freshly exposed sections using stainless steel tubes (5 cm diameter, 20 cm length) to prevent light exposure [28–30]. A total of 17 OSL samples were collected: 7 from GT profile (depths 1.7–14.2 m), 4 from BD profile (depths 1.8–8.1 m), and 6 from ZG profile (depths 1.9–12.3 m). Grain size samples were collected at 5 cm intervals, yielding 298 samples from GT, 166 from BD, and 265 from ZG profiles. For detrital zircon U-Pb analysis, 5 kg bulk samples representing 1 m stratigraphic thickness were collected from the middle section of each profile.

3.2. OSL Chronology

OSL measurements were conducted at the Luminescence Dating Laboratory, China University of Geosciences (Wuhan), using a Risø TL/OSL-DA-20 reader (Risø National Laboratory, Roskilde, Denmark) equipped with blue LED stimulation (470 nm) and 90Sr/90Y β-source irradiation [31]. Quartz grains (38–63 μm) were prepared following standard protocols [32]. Samples were pretreated with 10% HCl to remove carbonates, 30% H_2O_2 to remove organic matter, and 40% HF to dissolve quartz surfaces and eliminate feldspar contamination [33].

Equivalent doses (De) were determined using the single-aliquot regenerative-dose (SAR) protocol [34] with preheat at 260 °C for 10 s and cutheat at 220 °C for 5 s. Recent advances in luminescence dating methodology emphasize the importance of proper signal interpretation and statistical analysis for reliable age determination [35]. Dose rates were calculated from U, Th, and K concentrations measured by inductively coupled plasma mass spectrometry (ICP-MS), with cosmic dose rates estimated following Prescott and Hutton [36]. Water contents ranged from 11.69% to 19.62% with assumed uncertainties of ±5% to account for temporal variations. Age uncertainties (1σ) incorporate errors from both equivalent dose measurements and dose rate determinations.

3.3. Grain Size Analysis

Grain size distributions were measured to evaluate sediment transport dynamics and provenance signatures. Approximately 50 g samples from all three profiles were pretreated with 10% H_2O_2 to remove organic matter, 10% HCl to remove carbonates, and dispersed

with 0.05 M sodium hexametaphosphate. Analyses were performed using a Malvern Mastersizer 3000 (Malvern Panalytical, Malvern, UK) laser diffraction analyzer with a measurement range of 0.1–2000 μm. Results were classified into clay (<4 μm), fine silt (4–20 μm), coarse silt (20–63 μm), and sand (>63 μm) fractions, with proportions reported at 1σ uncertainty.

3.4. Detrital Zircon U-Pb Geochronology

Zircon separation from ~5 kg loess samples utilized heavy liquid separation (sodium polytungstate, density 2.9 g/cm^3) and magnetic separation using a Frantz magnetic separator. More than 2000 zircon grains were recovered from the bulk sample of each profile, from which 420 grains were randomly selected for U-Pb dating (totaling 1260 analyses across the three profiles). Separated heavy mineral fractions containing zircons of all grain sizes were mounted in epoxy resin following standard procedures for detrital zircon studies [37]. Polished grain mounts were imaged using scanning electron microscopy (SEM) cathodoluminescence (CL) to reveal internal structures and guide analytical spot selection.

U-Pb analyses were performed using an Agilent 7900 (Agilent, Santa Clara, CA, USA) quadrupole ICP-MS coupled with a 193 nm ArF excimer laser ablation system (GeoLas Pro), following recent methodological improvements in minimizing Pb loss effects during LA-ICP-MS analysis [38]. Random grain selection was employed to minimize bias, following best practices for detrital zircon geochronology [39]. Laser operating conditions included 5 Hz frequency, 24 μm spot size, and 5 J/cm^2 energy density. Helium was used as carrier gas to enhance transport efficiency.

Each analysis comprised 20 s background measurement and 40 s sample ablation. Zircon standard 91500 (1065.4 ± 0.3 Ma) served as the primary reference material with two analyses per 10 samples, while Plešovice zircon (337.13 ± 0.37 Ma) was used as secondary standard for accuracy monitoring [40,41]. Raw data processing utilized ICPMSDataCal (version 10.8, 2020) software for offline data selection, background correction, and standard calibration [42]. Common Pb correction employed the 208Pb method [43], with ages calculated using 206Pb/238U ratios for grains < 1000 Ma and 207Pb/206Pb ratios for grains > 1000 Ma. Analyses with >10% discordance or >10% error were rejected, with final ages reported at 2σ uncertainty.

Kernel density estimates (KDE) were generated using a Gaussian kernel with bandwidth = 15 Ma. Sensitivity tests using bandwidths of 10 Ma and 20 Ma yielded consistent peak positions (within ±5 Ma), indicating robustness.

3.5. Comparative Dataset Compilation

Published U-Pb age datasets from the Chinese Loess Plateau and potential source regions were compiled for comparative analysis, refer to Supplementary Materials Table S1 for data and sources. To ensure statistical reliability, datasets were grouped to achieve sufficient size for detecting age populations representing > 5% of grains at 95% confidence level [44]. Source data were grouped by major geomorphological settings, including the Three Gorges-Yangtze (TGY), Sichuan Basin (SCB), Western Loess Plateau (WLP), Tarim Basin (TB), Mu Us Desert (MUD), Qaidam Basin (QB), Songpan-Ganzi (SPG), Tengger Desert (TGD), Otindag, and Korqin sandy lands and other Northern China sandy lands (Table S1).

4. Results and Analysis

4.1. OSL Chronology of Wushan Loess

A total of 17 samples from the GT, BD, and ZG profiles were analyzed using OSL dating at approximately 2 m intervals to establish a robust chronological framework for

Late Pleistocene deposition (Figure 2, Table 1). All OSL signals decayed to background levels within 10 s of blue light stimulation, indicating good signal sensitivity (Figure 2a–c). Dose–response curves generated using the single-aliquot regenerative-dose (SAR) protocol displayed characteristic upward trends without saturation within the measured dose range (Figure 2d–f), confirming the reliability of equivalent dose determinations [45].

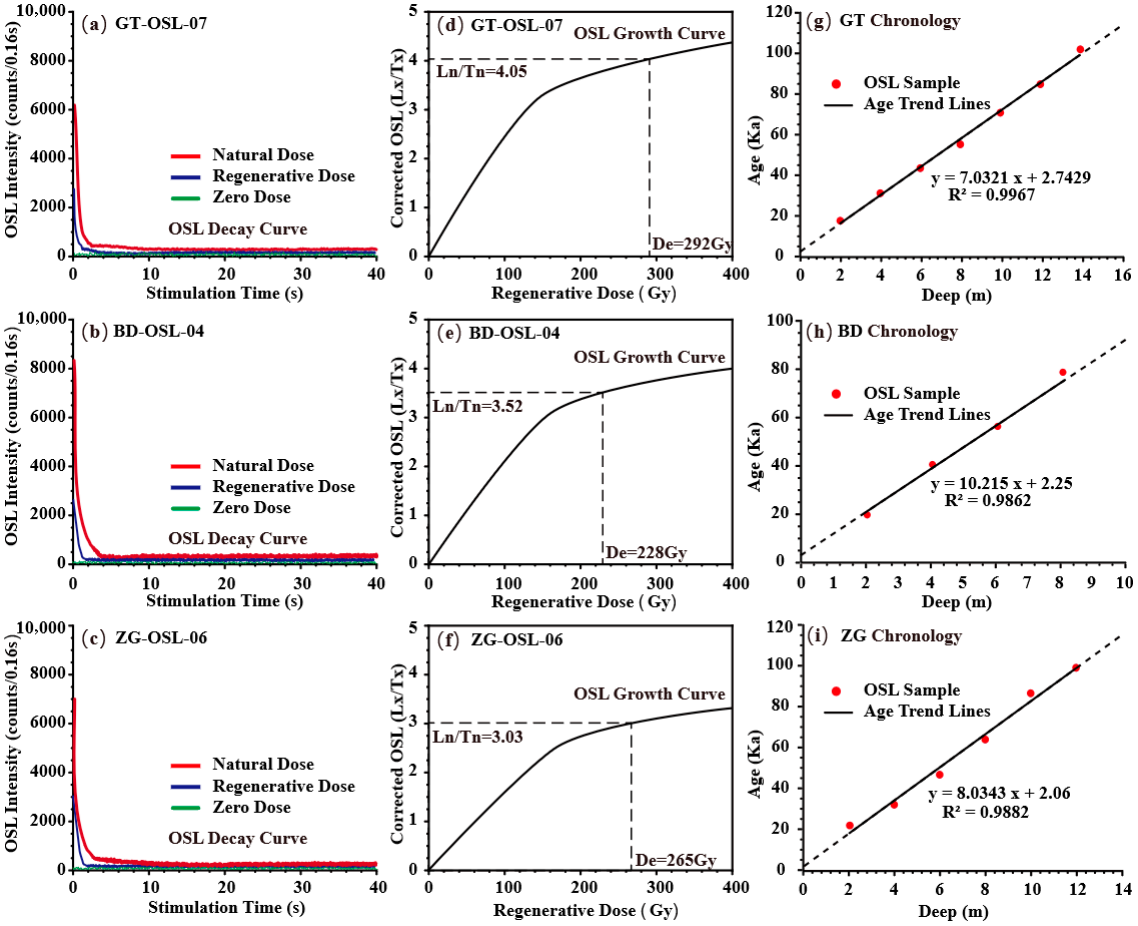


Figure 2. OSL dating results for the Wushan Loess profiles at GT, BD, and ZG sites, illustrating signal characteristics and chronological framework. (**a**–**c**) Normalized OSL intensity decay curves for the natural dose (red), regenerative dose (blue), and zero dose (green) at representative samples (GT-OSL07, BD-OSL04, ZG-OSL06), demonstrating quartz signal suitability for dosimetry. (**d**–**f**) Dose–response growth curves fitted with single saturating exponential functions (Ln-Tn model). (**g**–**i**) Age-depth models plotting OSL ages (red/black dots) against stratigraphic depth.

Equivalent doses (De) ranged from 35.96 to 237.04 Gy, with corresponding dose rates of 1.81–2.59 Gy/ka, yielding OSL ages with uncertainties of ±1.20–4.92 ka. Age-depth models constructed using linear interpolation of OSL ages (Figure 2g–i) were adjusted for potential depositional hiatuses identified through stratigraphic analysis [46].

The GT profile (15 m thick) spans 18.1 ± 1.20 ka (1.7 m depth, $L_{1\text{-}1}$) to 103.8 ± 5.11 ka (14.2 m depth, $L_{1\text{-}3}$), covering approximately 85.7 ka (MIS 5 to MIS 2). A carbonate nodule horizon ($L_{1\text{-}2}$) at 3.8–5.2 m depth corresponds to ~33.3–43.4 ka (MIS 3). The calculated mean sedimentation rate is 14.58 cm/ka. The BD profile (8 m thick) ranges from 21.3 ± 1.90 ka (1.8 m depth, $L_{1\text{-}1}$) to 89.2 ± 3.97 ka (8.1 m depth, S_1), with a transitional loess layer (LT) at 2.2 m dating to ~25.3 ka (MIS 2). The profile represents ~67.9 ka (MIS 5 to MIS 2) with a mean sedimentation rate of 9.27 cm/ka. The ZG profile (13 m thick) extends from 22.1 ± 1.01 ka (1.9 m depth, $L_{1\text{-}1}$) to 98.7 ± 4.92 ka (12.3 m depth, S_2), with paleosol layer S_1

at 9.3–10.5 m corresponding to ~76.0–85.5 ka (MIS 5). This profile spans ~77.4 ka (MIS 5 to MIS 2) with a mean sedimentation rate of 13.57 cm/ka.

Table 1. OSL Dating Results for Wushan Loess.

Sample ID	Grain Size (μm)	Sample Level (m)	U (ppm)	Th (ppm)	K (%)	Water Content (%)	Dose Rate D (Gy/ka)	Equivalent Dose De (Gy)	Age (ka)
GT-OSL-01	38–63	1.7	1.939	7.074	1.296	18.69%	1.99 ± 0.10	35.96 ± 5.03	18.1 ± 1.20
GT-OSL-02	38–63	3.8	2.089	7.174	1.47	13.61%	2.24 ± 0.09	71.58 ± 7.16	31.9 ± 1.41
GT-OSL-03	38–63	5.9	2.094	7.837	1.615	19.62%	2.27 ± 0.08	100.6 ± 9.05	44.4 ± 2.26
GT-OSL-04	38–63	8.3	2.113	7.425	1.474	11.69%	2.28 ± 0.07	128.24 ± 11.54	56.3 ± 2.35
GT-OSL-05	38–63	9.8	2.161	7.371	1.488	14.31%	2.23 ± 0.06	160.9 ± 19.31	72.1 ± 3.80
GT-OSL-06	38–63	12.1	2.763	8.599	1.412	18.35%	2.28 ± 0.05	196.86 ± 25.59	86.4 ± 4.32
GT-OSL-07	38–63	14.2	2.857	8.806	1.283	16.51%	2.24 ± 0.04	237.04 ± 33.19	103.8 ± 5.11
BD-OSL-01	38–63	1.8	2.713	7.733	1.284	15.77%	2.23 ± 0.09	47.55 ± 6.18	21.3 ± 1.90
BD-OSL-02	38–63	4.1	2.54	7.889	1.266	17.76%	2.14 ± 0.07	89.9 ± 8.99	42.1 ± 2.46
BD-OSL-03	38–63	6.2	2.447	6.918	1.005	19.09%	1.81 ± 0.06	113.62 ± 10.23	62.7 ± 3.02
BD-OSL-04	38–63	8.1	2.404	6.766	0.993	15.79%	1.83 ± 0.05	162.8 ± 19.54	89.2 ± 3.97
ZG-OSL-01	38–63	1.9	2.296	7.127	1.185	15.67%	2.03 ± 0.08	44.84 ± 5.83	22.1 ±1.01
ZG-OSL-02	38–63	3.9	3.058	8.104	1.081	17.70%	2.11 ± 0.08	67.89 ± 6.79	32.2 ± 1.45
ZG-OSL-03	38–63	6.1	2.756	8.517	1.782	18.87%	2.59 ± 0.09	120.89 ± 10.88	46.7 ± 2.48
ZG-OSL-04	38–63	7.9	1.965	6.569	1.461	17.06%	2.08 ± 0.06	132.51 ± 11.93	63.8 ± 3.06
ZG-OSL-05	38–63	10.2	1.83	7.916	1.557	14.33%	2.25 ± 0.06	194.34 ± 25.26	86.3 ± 4.39
ZG-OSL-06	38–63	12.3	2.238	8.113	1.179	16.07%	2.02 ± 0.04	197.21 ± 27.61	98.7 ± 4.92

The OSL chronology indicates continuous loess deposition from ~103 ka to ~18 ka, coinciding with enhanced East Asian winter monsoon activity during glacial periods [47]. Sedimentation rates across all profiles range from 9.27 to 14.58 cm/ka, consistent with other Chinese loess sequences from similar latitudes [48].

4.2. Grain Size Analysis and Depositional Characteristics

Field observations of the GT, BD, and ZG profiles reveal that the Wushan Loess consists of homogeneous, massive silt layers with uniform light yellowish-brown coloration and well-developed vertical jointing. The absence of horizontal cross-stratification, ripple marks, or upward-fining sequences typical of fluvial or alluvial deposits indicates minimal post-depositional hydraulic reworking [49].

The Wushan Loess is dominated by silt-sized particles (4–63 μm), comprising 72%, 75%, and 78% of the GT, BD, and ZG profiles, respectively. Modal grain sizes consistently fall within 20–25 μm, characteristic of aeolian loess deposits [50]. Sand (>63 μm) and clay (<4 μm) fractions represent 9.70%, 9.60%, 6.62% and 16.25%, 12.34%, 15.43%, respectively, across the three profiles (Table 2).

Table 2. Grain Size Characteristics of Wushan Loess Profile.

Profiles		<4 μm (%)	4–20 μm (%)	20–63 μm (%)	>63 μm (%)
GT n = 298	Maximum	17.82	34.95	44.73	11.50
	Minimum	14.35	29.12	40.28	8.25
	Mean	16.25	32.18	41.87	9.70
BD n = 166	Maximum	13.67	31.84	51.89	12.60
	Minimum	10.43	26.15	46.32	7.10
	Mean	12.34	29.15	48.91	9.60
ZG n = 265	Maximum	16.94	30.78	52.65	8.63
	Minimum	13.21	25.47	47.19	5.13
	Mean	15.43	28.27	49.68	6.62

Table 1 shows the grain size characteristics of Wushan Loess Profile, which reveal important provenance signatures. Fine particles (<20 μm, including clay <4 μm) account

for 41%–48% (GT 48.4%, BD 41.5%, ZG 43.7%) of the sediments across all profiles, are capable of long-distance aeolian transport and likely originate from the Loess Plateau and other distal source regions [51]. Conversely, coarse silt (20–63 μm), averaging 41%–50%, may reflect proximal contributions from the upper Yangtze River basin, as such particles typically undergo shorter transport distances [52,53]. These grain size variations, combined with OSL ages, can reflect the different aeolian dynamics experienced by Wushan Loess at different stages of the Late Pleistocene (Figure 3).

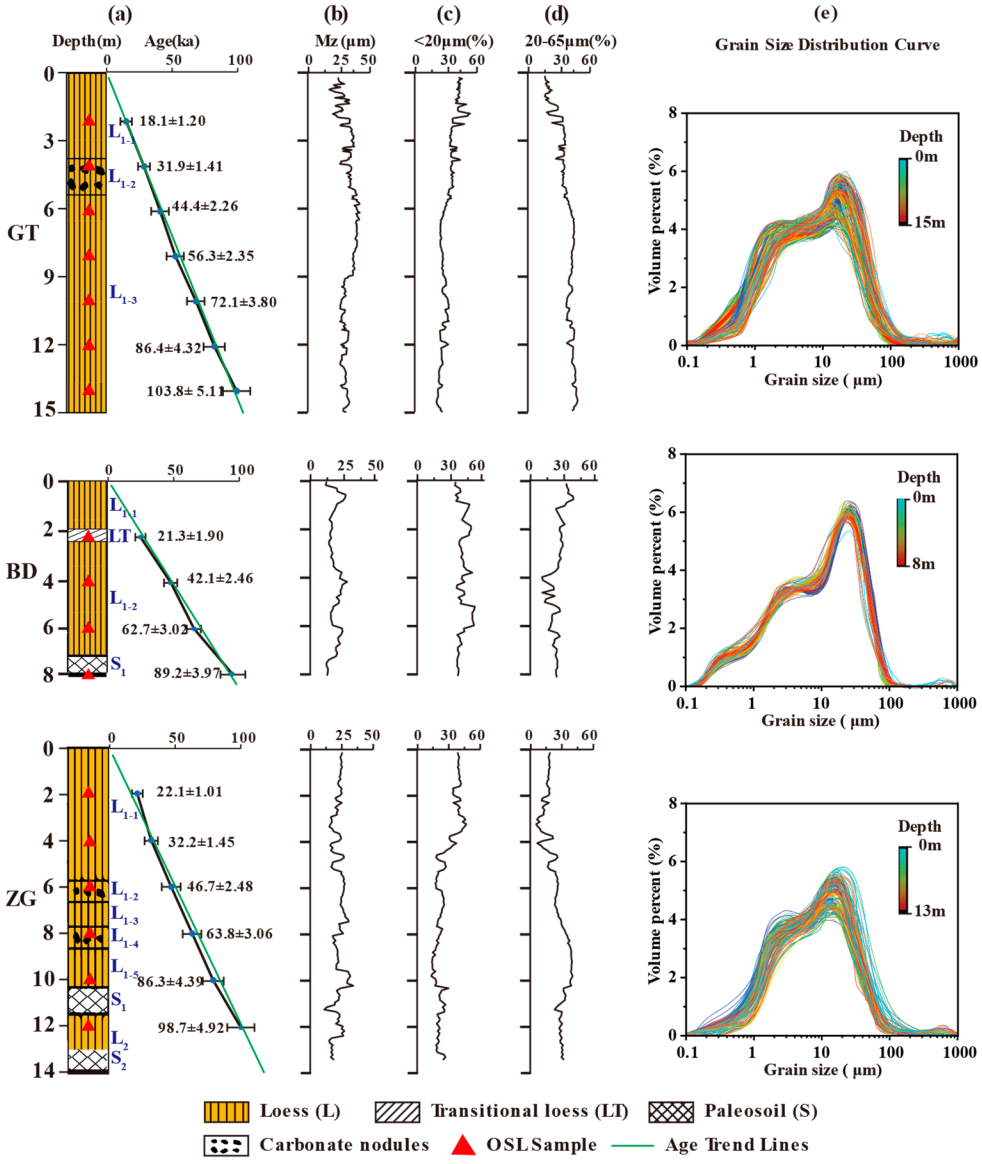


Figure 3. Age-depth models and grain size distributions of the Wushan Loess profiles. (**a**) Age-depth plots integrating OSL ages (red triangles) and stratigraphic units, with linear regression trends (green lines) constraining deposition to 18–103 ka (Marine Isotope Stages 2–5). (**b**–**d**) Percentage contents of different grain size fractions. (**e**) Grain size distribution curve for three profiles.

4.3. Detrital Zircon Morphology and U-Pb Ages

Following recent best practices for large-n detrital zircon datasets [54], our sample sizes exceed the recommended minimum of 300 grains required to detect age components representing ≥ 5% of the population at 95% confidence level. Age calculations followed established protocols: 206Pb/238U ratios for grains < 1000 Ma and 207Pb/206Pb ratios for grains > 1000 Ma [55].

Representative cathodoluminescence (CL) images of detrital zircon grains from the GT, BD, and ZG profiles are shown in Figure 4a–f. Most zircons exhibit rounded to sub-rounded morphologies with minor euhedral forms, indicating substantial aeolian transport. To ensure statistical reliability, approximately 420 zircon grains were analyzed from each profile, totaling 1260 analyses. After filtering for concordance (>90% agreement between 206Pb/238U and 207Pb/206Pb ages), 1189 valid ages were obtained (GT: 406 grains; BD: 391 grains; ZG: 402 grains).

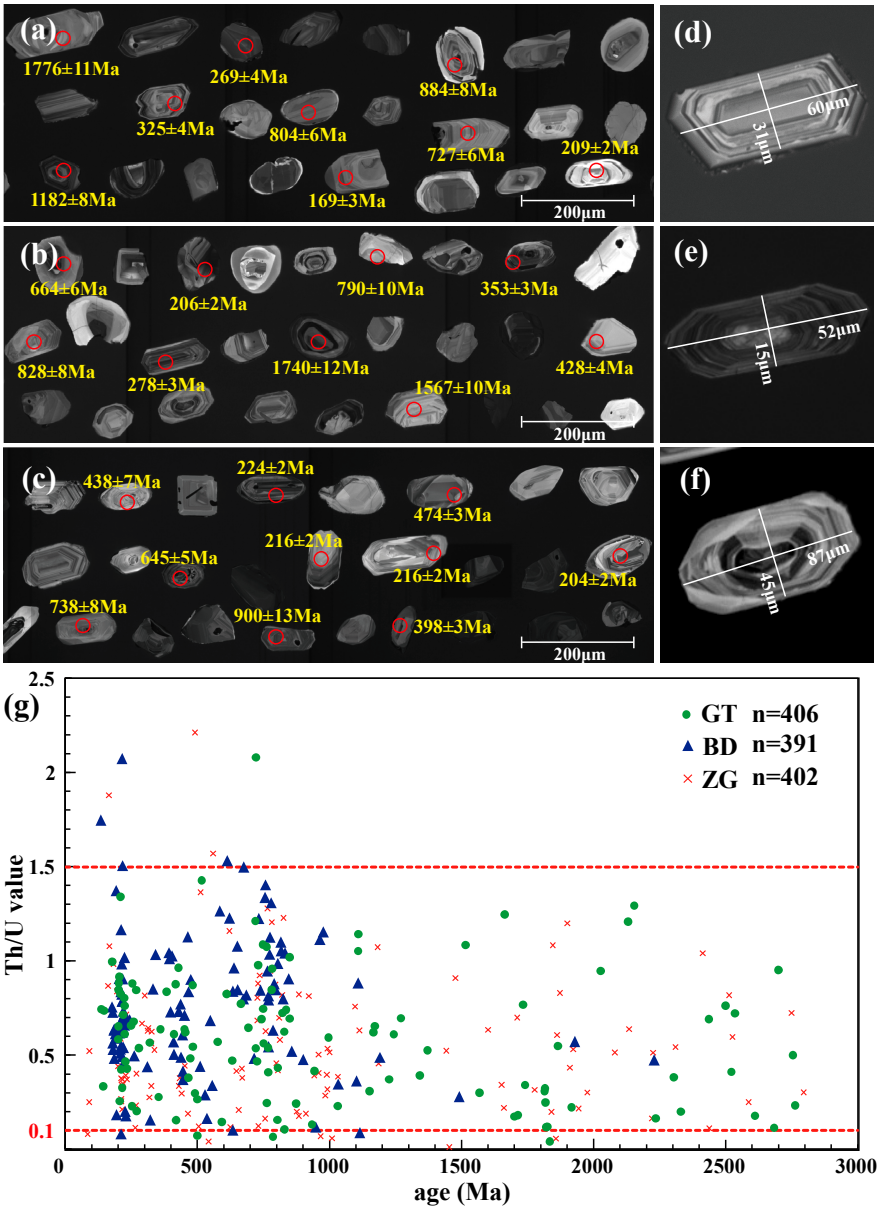


Figure 4. Cathodoluminescence (CL) images of representative detrital zircons from the Wushan Loess profiles and Th/U ratios versus U-Pb age. (**a**–**f**) depict characteristic morphologies of zircons, such as zoned, oscillatory, and sector-zoned crystals. (**g**) features a scatter plot that differentiates provenance signatures through Th/U partitioning. Note: Red circles indicate test points.

Th/U ratios, commonly used to infer zircon origin, predominantly range from 0.1 to 1.5, indicating magmatic origins, with few metamorphic zircons (Th/U < 0.1) present (Figure 4g). CL images reveal characteristic oscillatory zoning patterns (Figure 4a–f), supporting interpretation of U-Pb ages as igneous crystallization ages [56].

The large sample sizes (~400 zircons per profile) and random sampling methodology significantly enhance the precision of age spectra characterization and statistical confidence [57]. Kernel Density Estimation (KDE) analysis (Figure 5) reveals highly consistent major age peaks (210–220 Ma, 450–500 Ma, 772–791 Ma, 1830–1873 Ma) across all profiles, confirming that sub-sampling has adequately captured the primary source region signals. Proportions of age components were quantified by integrating KDE probability densities over 10 Ma age bins (Gaussian bandwidth: 15 Ma), with uncertainties (±2%) derived from bootstrap resampling (n = 1000 iterations). The statistical robustness achieved through large sample sizes allows confident identification of minor age components representing as little as 2%–3% of the total population [58]. Inter-profile variations are minor (e.g., 160–260 Ma grains: GT 32% ± 2%, BD 30% ± 2%, ZG 29% ± 2%) and likely reflect subtle changes in transport pathways or wind dynamics during deposition, possibly influenced by local topographic effects in the Three Gorges region.

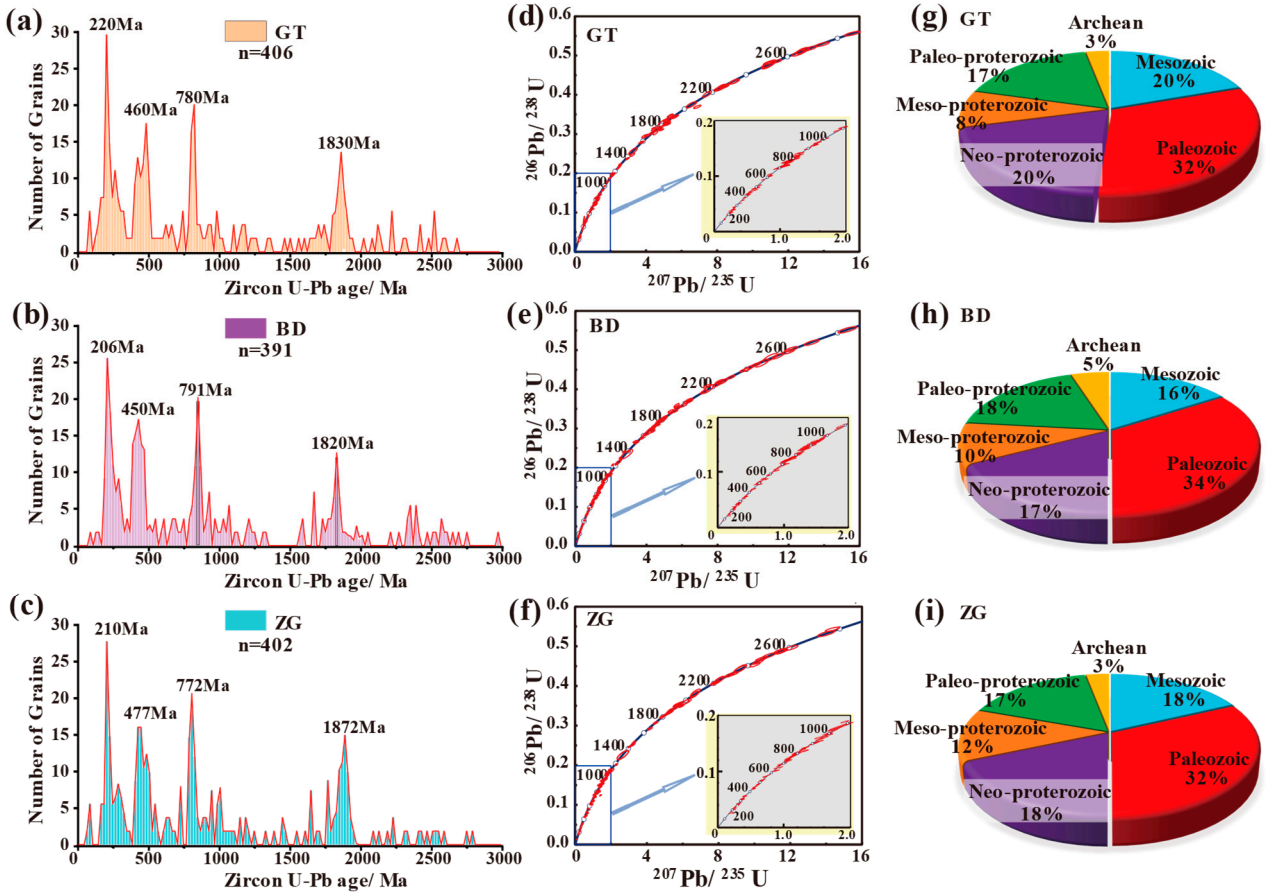


Figure 5. Detrital zircon U-Pb age distributions and geological era proportions in the Wushan Loess profiles. (**a**–**c**) Kernel density estimates (KDE) and histograms of U-Pb ages for the GT, BD, and ZG profiles. (**d**–**f**) Cumulative probability plots of U-Pb ages. (**g**–**i**) Pie charts illustrating era-based proportions, with dominant contributions from the Mesozoic (16%–20%), Paleozoic (32%–34%), Neoproterozoic (17%–20%), and Paleoproterozoic (17%–18%).

The results demonstrate the following: (1) overall similarity among the three profiles (GT, BD, ZG), indicating consistent provenance throughout the glacial-interglacial cycle. Sample ages predominantly fall within 200 ± 5 to 900 ± 15 Ma, representing >60% of all zircons, with <10% >2000 Ma. (2) Four distinct age peaks are evident in all samples: primary peaks at Triassic, ~220 Ma (GT), ~206 Ma (BD), and ~210 Ma (ZG); secondary peaks at Neoproterozoic, ~780 Ma (GT), ~791 Ma (BD), and ~772 Ma (ZG); tertiary peaks

at Ordovician, ~460 Ma (GT), ~450 Ma (BD), and ~477 Ma (ZG); and quaternary peaks at Paleoproterozoic, ~1830 Ma (GT), ~1820 Ma (BD), and ~1872 Ma (ZG). (3) Minor inter-profile variations exist: GT and ZG show higher proportions (15%–16% vs. 11% for BD) in the 700–800 Ma range; ZG displays 7% in the 1800–1900 Ma range (vs. 3% for GT and 5% for BD); ZG contains <1% >2500 Ma grains (vs. 2% for GT and 3% for BD). These differences likely stem from topographic variations: the GT and ZG profiles are situated on terraces flanking both banks of the Yangtze River, whereas the BD profile occupies a higher-elevation river valley setting.

5. Discussion

5.1. Grain Size Evidence for Aeolian Genesis of Wushan Loess

The grain size distribution curves of the three Wushan Loess profiles show consistent patterns characterized by asymmetric bimodal distributions (Figure 3), with primary modes dominated by silt particles and maximum coarse silt content. Modal grain sizes fall within the 4–63 μm range, with the rate of decrease toward coarser particles being faster than toward finer particles. Extensive research indicates that particles in the 10–50 μm size range are most susceptible to atmospheric suspension and constitute the primary target for aeolian transport [59]. Particles smaller than 20 μm can be transported by wind over thousands of kilometers, while transport coefficients decrease with increasing grain size, resulting in progressively poorer atmospheric suspension capabilities. Particles larger than 63 μm generally cannot remain airborne and are typically transported only through saltation [60].

The predominance of silt-sized particles in the grain size curves (Figure 3e) strongly supports an aeolian origin for the Wushan Loess [61]. Additionally, the mountainous terrain setting of the Wushan Loess exhibits particularly pronounced aeolian deposition characteristics. Some layers contain coarse particles, such as individual samples near 6 m depth in the BD profile showing small peaks at >500 μm, potentially resulting from mixing of nearby mountain-derived material during periods of enhanced wind activity. Similar occurrences in the GT and ZG profiles reflect general characteristics of aeolian deposition in mountainous terrain.

Grain size pattern analysis has been widely applied to aeolian deposits. In this study, grain size data from fluvial sediments in the middle and lower reaches of the Yangtze River, as well as from typical aeolian loess and the Xiashu Loess [59,61,62], were collected for comparative analysis using C-M, A-M, and L-M grain size diagrams (where C represents the grain size corresponding to the 1% tail on the cumulative curve, M is the median grain size, and A and L are the percentages of particles smaller than 4 μm and 31 μm) (Figure 6a–c).

In addition, we also compared the grain size parameters σ, sk, and kg represent standard deviation, skewness, and kurtosis of the grain size distribution, respectively. The grain size parameters indicate moderate to poor sorting (σ =2.26 on average), positive skewness (SK = 0.21), and variable kurtosis (0.52–1.38), all consistent with wind-transported sediments [53] (Figure 6d–f). These parameters generally possess diagnostic significance for genesis and depositional environment interpretation. The Wushan Loess grain size parameter scatter plots differ significantly from modern fluvial sediments but show remarkable consistency with the distribution fields of Xiashu Loess from the Chaohu Basin, indicating similar aeolian origins while differing from fluvial genesis [62].

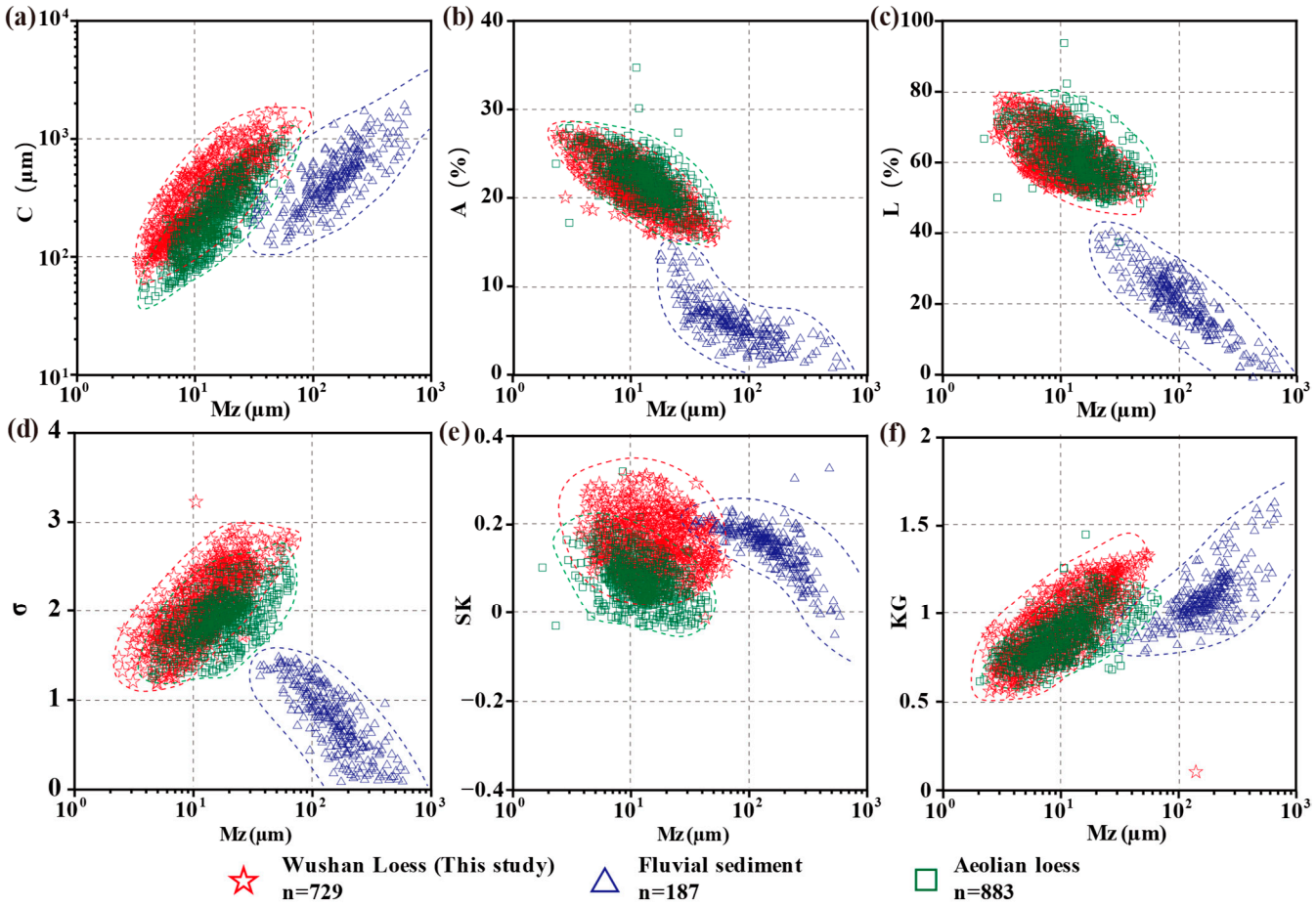


Figure 6. Comparison of grain size parameters among the Wushan Loess, fluvial sediments, and aeolian loess deposits. In the figure, Mz represents the median grain size, (**a**) C is the particle size at the 1% point on the cumulative curve, (**b**) A is the percentage of particles smaller than 4 μm, (**c**) L is the percentage of particles smaller than 31 μm, (**d**) σ is the standard deviation of particle size, (**e**) SK is skewness, and (**f**) KG is kurtosis. Note: The grain size data of Wushan Loess are from this study, while fluvial sediments and aeolian loess deposits are from previous studies [58–61].

Recent advances in provenance studies of loess deposits in the East Asian monsoon boundary zone emphasize the critical importance of grain size analysis for paleoclimatic reconstruction, particularly in understanding variations in climate and wind regimes [63]. Our results demonstrate that the Wushan Loess exhibits characteristics consistent with typical aeolian transport, supporting its interpretation as a wind-blown deposit.

5.2. Mixed Provenance Model Based on U-Pb Age Signatures

Comparative analysis of detrital zircon U-Pb age data between the Wushan Loess and potential source regions provides valuable insights into provenance relationships (Figure 7). To ensure robust source data (>300 samples) and mitigate biases from individual profiles, we integrated data from multiple profiles within the source regions. Standardized processing (e.g., KDE adaptive bandwidth) and Monte Carlo simulations (n = 1000) were applied to reduce uncertainties, enhancing the representativeness of the source data [58,59]. The age distribution of the Wushan Loess exhibits clear mixed-source characteristics, as revealed by probability density plots comparing samples from potential source regions including the Sichuan Basin, Three Gorges, Loess Plateau, Tarim Basin, Qaidam Basin, Tengger Desert, Otindag Sandy Land, Songpan-Ganzi, Korqin Sandy Land, and Mu Us Desert.

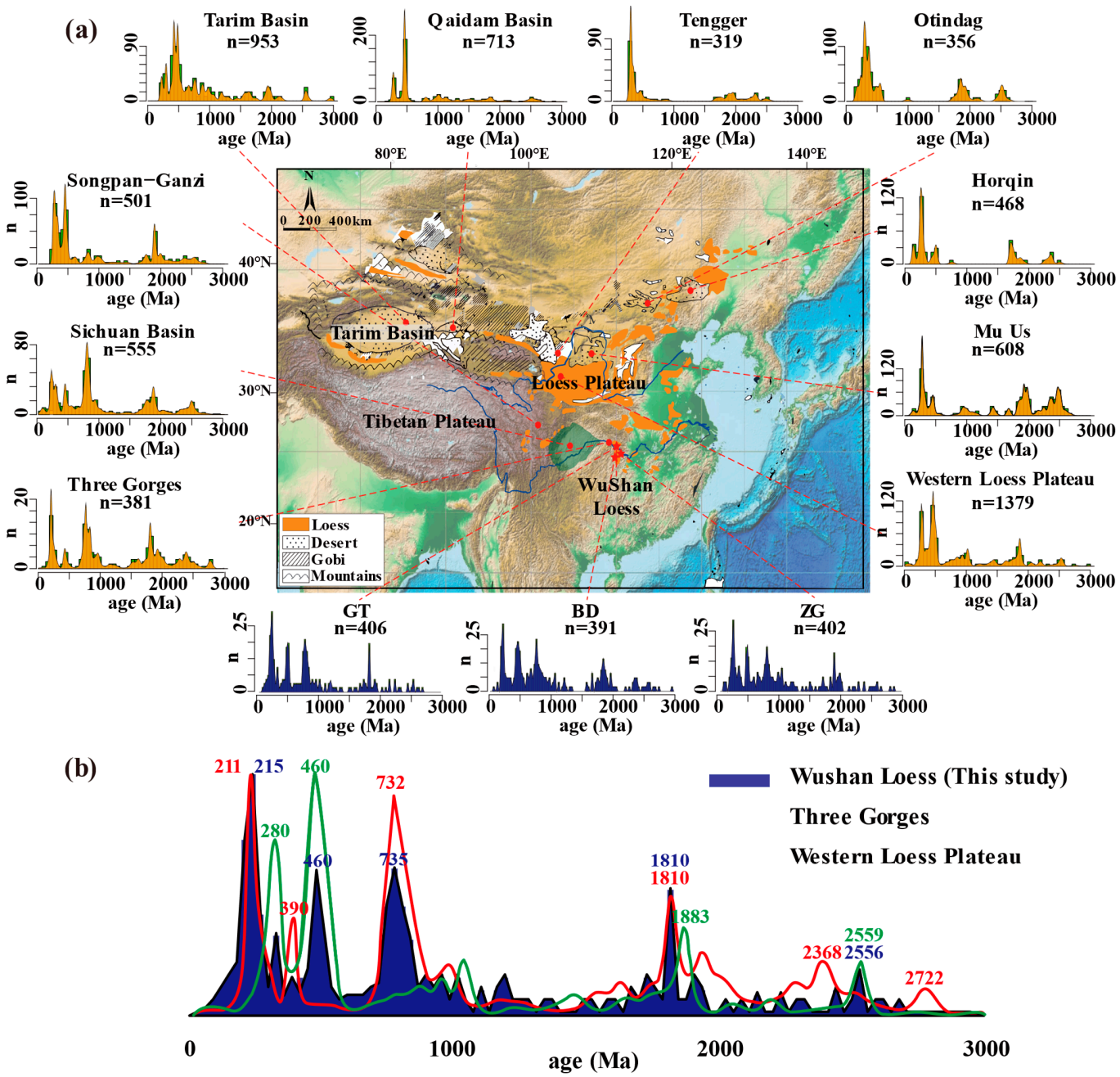


Figure 7. Comparison of detrital zircon U-Pb age spectra between the Wushan Loess and potential source regions. (**a**) Regional map of East Asia illustrating the spatial distribution of loess deposits, Gobi deserts, and major mountain ranges as potential source areas, along with their characteristic zircon U-Pb age signatures. (**b**) Similarity comparison of kernel density estimation (KDE) plots for U-Pb age distributions (Ma) from Wushan Loess profiles against the Three Gorges-Yangtze region and Western Loess Plateau. Note: The U-Pb data of zircon from the Wushan Loess were obtained in this study, and the data sources for potential source areas are listed in Table S1.

The dominant 210 ± 50 Ma age peak in all Wushan Loess profiles corresponds to Indosinian magmatic activity in the Three Gorges region and broader Yangtze Craton, indicating significant contributions from local or regional sources within the Yangtze River drainage basin [64]. Secondary peaks at 730 ± 50 Ma align with characteristic age signatures of the western Loess Plateau, suggesting contributions from long-distance aeolian transport by the Late Pleistocene East Asian winter monsoon [65].

Recent studies on the oldest Xiashu Loess and Xuancheng loess in southern China have revealed similar mixed provenance patterns, with implications for dust transport and dust proxies of the East Asian winter monsoon [66]. These findings support the interpretation that southern Chinese loess deposits, including the Wushan Loess, receive contributions from both proximal and distal sources.

Multi-Dimensional Scaling (MDS) analysis quantitatively demonstrates source similarities, with the Wushan Loess showing smaller K-S distances (0.12–0.18) with the Three Gorges region, Sichuan Basin and Loess Plateau compared to larger distances (0.35–0.42) with the Qaidam Basin, Tarim Basin and other northern desert and Gobi regions (Figure 8). This supports the dominant contribution of proximal aeolian dust sources. The age peaks from Three Gorges (Figure 7a) indicate that the Three Gorges region is primarily controlled by the Yangtze Craton and Huangling Dome, showing high consistency with the Wushan Loess age patterns.

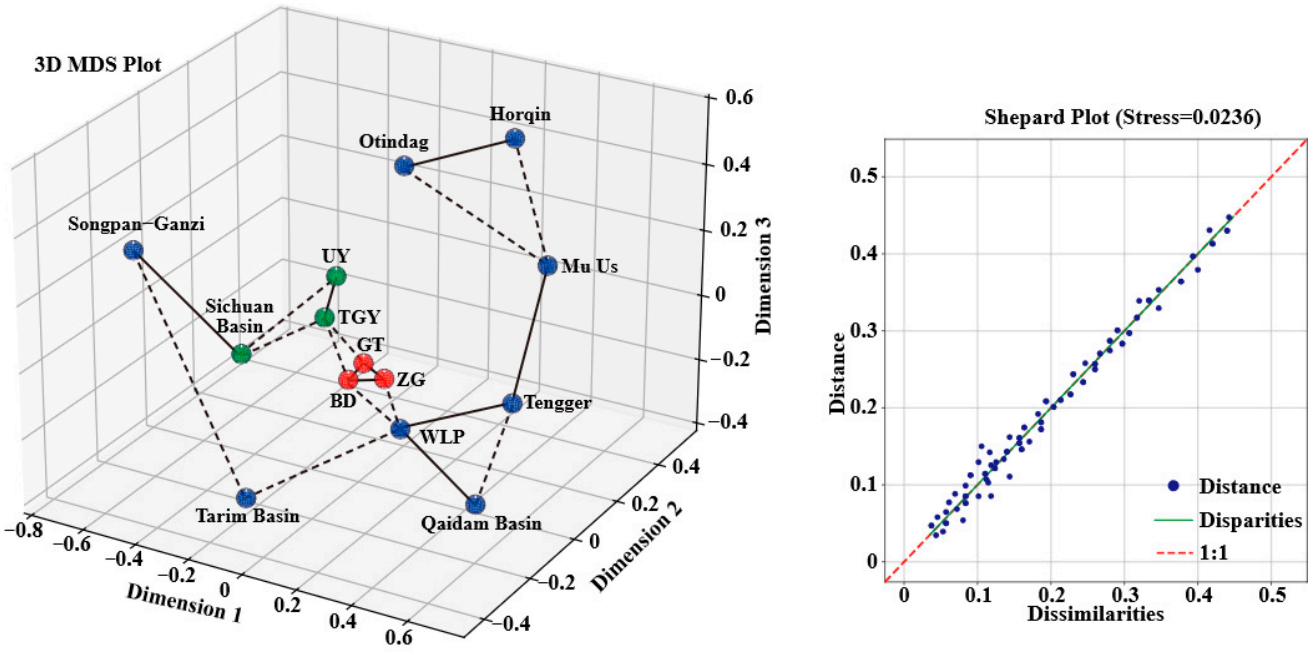


Figure 8. Three-dimensional Multi-Dimensional Scaling (MDS) plot of detrital zircon U-Pb age distribution similarities between Wushan Loess profiles and potential source regions. In 3D MDS plot, red points denote samples from this study (GT, BD, ZG); green points represent Yangtze River basin sources (TGY: Three Gorges-Yangtze; UY: Upper Yangtze; SCB: Sichuan Basin); blue points indicate northern Chinese sources (WLP: Western Loess Plateau; Mu Us; Tengger; Horqin; Otindag; Songpan-Ganzi; Tarim Basin; Qaidam Basin). In the Shepard plot, solid lines signify primary correlations, while dotted lines denote secondary correlations (Borg and Groenen, 2003) [67,68].

5.3. Quantitative Estimation of Material Sources

The Non-negative least squares (NNLS) unmixing was implemented using Python 3.11 (SciPy optimize.nnls), with input probability density functions normalized to unity. Leave-one-out tests and 1000 bootstrap iterations were used to estimate model uncertainty. Misfit between modeled and observed spectra was quantified by the Kolmogorov–Smirnov D-statistic. Calculation methods and procedures are detailed in the Supplementary Information (SI).

NNLS unmixing analysis yields quantitative estimates of source contributions: proximal sources from the Three Gorges and upper Yangtze regions (TGY) account for approximately ~42.5%, the Loess Plateau for about ~26.6%, the Sichuan Basin for relatively minor amounts (~22.5% combined), and northern desert endmembers (e.g., Mu Us and

Tengger) for negligible contributions (<10%) (Figure 9). These results align with grain size analyses revealing elevated coarse silt content—where recycling from proximal sources can simultaneously contribute both clay and coarse silt, whereas distal sources typically only supply fine particles (<20 μm)—indicating which indicates substantial proximal inputs, and they account for the coexistence of primary peaks at 200–220 Ma and secondary peaks at 400–500 Ma in the mixed zircon U-Pb age spectra.

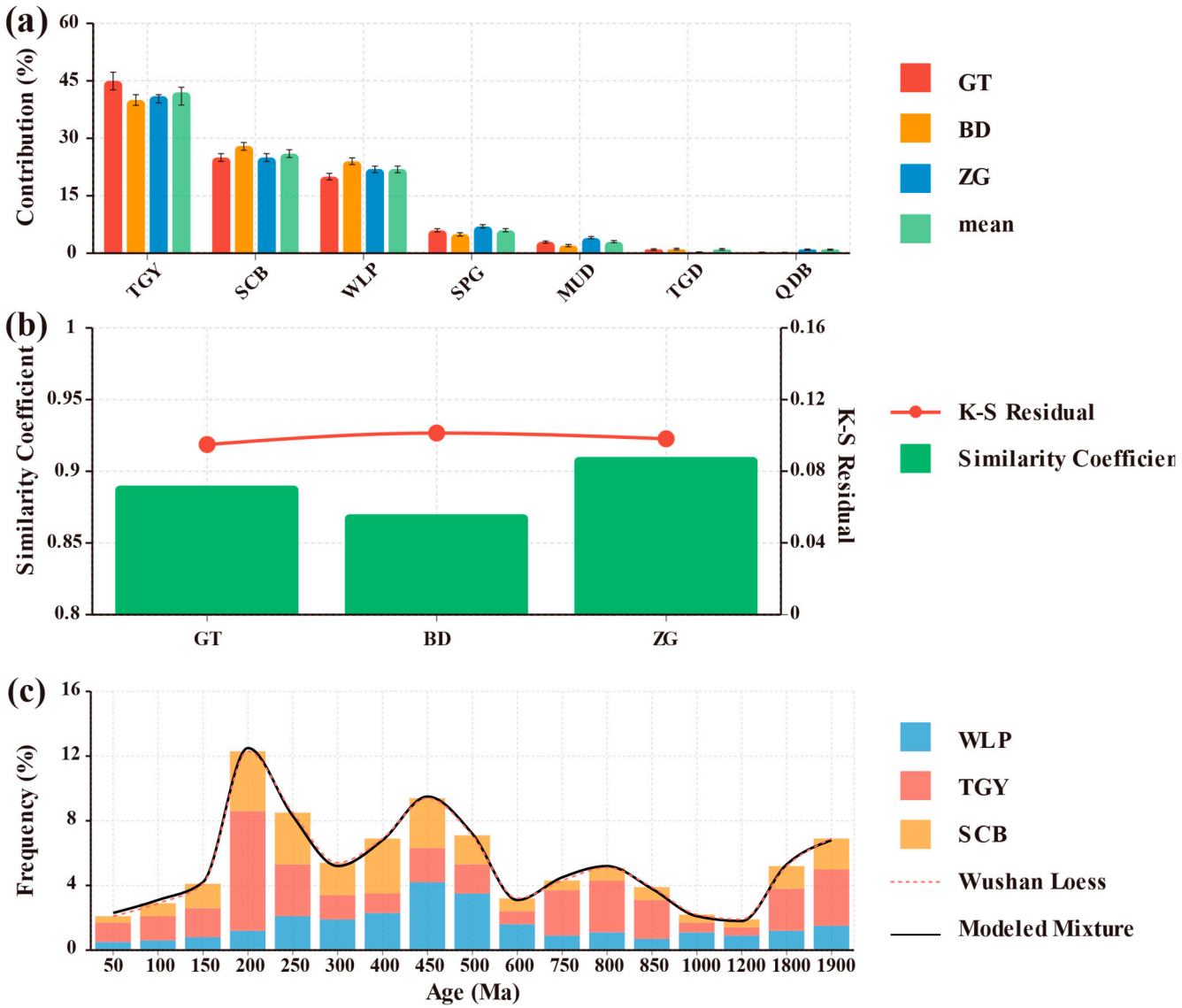


Figure 9. NNLS unmixing results for Wushan Loess provenance analysis. (**a**) Quantitative source contributions for three loess profiles (GT, BD, ZG) showing proximal-dominated provenance with 68 ± 5% from the upper Yangtze River basin (TGY + SCB) and 32 ± 5% from distal sources (WLP, SPG, MUD, others). Error bars represent ±1σ standard deviations from bootstrap resampling (n = 1000). (**b**) Validation of NNLS results showing high similarity coefficients (0.87–0.91) between observed and reconstructed distributions, and low K-S residuals (0.089–0.095) indicating excellent model fits. (**c**) Age distribution comparison for the GT profile showing good correspondence between observed Wushan Loess ages (black line) and modeled mixture (red dashed line). Stacked bars illustrate the contribution of different source regions to the detrital zircon U-Pb age spectrum. The dominant 200–220 Ma peak reflects strong TGY control, while the 450–500 Ma and 750–800 Ma peaks indicate significant contributions from Loess Plateau and recycled Yangtze basin sources, respectively.

5.4. Transport Pathways and Depositional Mechanisms

Comprehensive integration of U-Pb geochronology, grain size analysis, and multi-dimensional scaling results reveals that the material sources of the Wushan Loess can be characterized by a proximal-dominated pathway: primarily from proximal materials in the upper-middle Yangtze River basin and Three Gorges region, with additional contributions from distal materials from the Loess Plateau and northwestern deserts and Gobi regions (Figure 10).

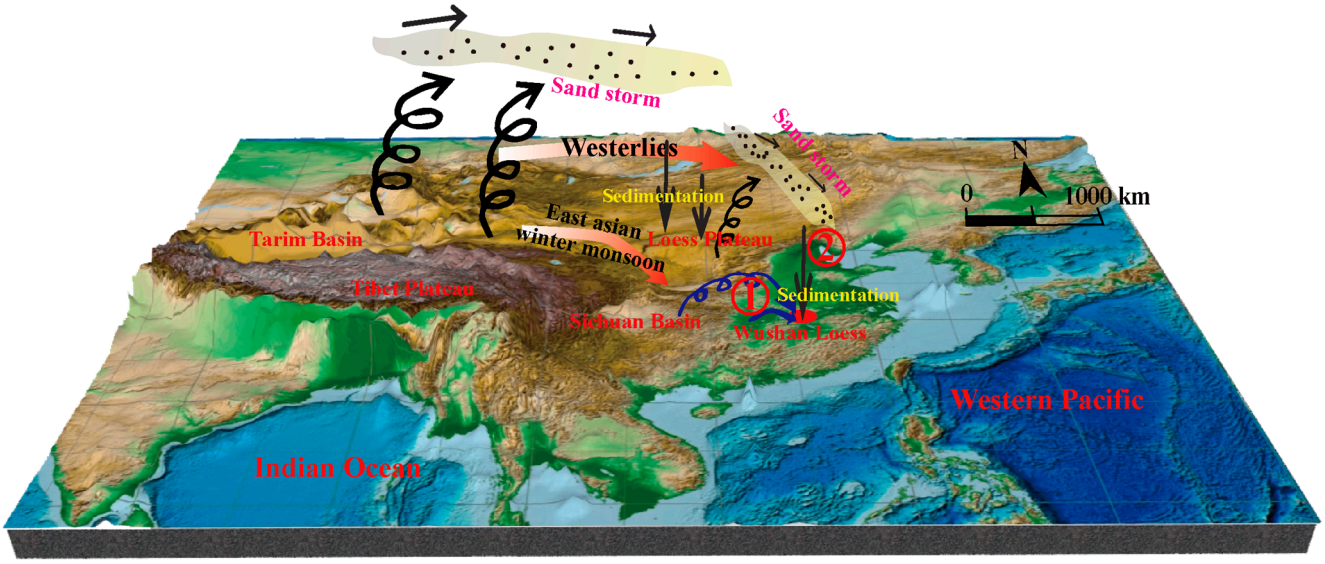


Figure 10. Depositional model for the Wushan Loess. In the diagram, pathway ① denotes proximal sourcing via the Three Gorges region and upper Yangtze River basin, while pathway ② represents distal sourcing primarily from the Loess Plateau and northern Chinese arid zones.

Proximal materials are primarily derived through local valley winds from exposed surfaces, floodplains, and Yangtze River terraces in the Three Gorges region, deposited via short-distance (kilometers to tens of kilometers) aeolian transport to the Wushan area. Distal materials are transported from the northwest through upper-level westerly circulation and East Asian winter monsoon over long distances to the study region [67].

The deposition of Wushan Loess is influenced by the valley topography of the Wushan Mountains, creating accommodation space on river terraces. The Yangtze River erodes and redistributes sediments during high-flow periods while exposing floodplains during low-water stages, providing source materials for Wushan Loess accumulation. This interaction has resulted in the unique detrital zircon U-Pb age characteristics of the Wushan Loess, exhibiting both prominent signals from proximal Yangtze River basin materials and secondary signatures from distal Loess Plateau and northwestern desert sources, reflecting mixed genesis characteristics [68].

5.5. Implications for Climate and Atmospheric Circulation Evolution

The formation of extensive and thick aeolian sediments depends on three main conditions: (1) supply of loose clastic materials, (2) strong surface winds, and (3) favorable topographic conditions [69]. Since the Late Pleistocene Last Glacial period, northern China experienced prolonged aridity, leading to expansion of desert and Gobi landscapes. This climate change created ideal conditions for dust particle formation, which accumulated in southern China with assistance from the East Asian monsoon. The topography of the Wushan region further promoted loess deposition.

OSL chronology indicates that Wushan Loess formation occurred from approximately 103 ka to 18 ka, demonstrating that East Asia experienced cold, arid, and windy periods during this interval (Figure 9). Since the Late Pleistocene, global climate cooling trends likely accelerated sedimentation rates and expanded the range of loess plateau formation [70–73]. Analysis of Wushan Loess basal ages helps reconstruct the historical extent of loess accumulation across different geological periods in China.

The relationship between Asian summer monsoon and westerlies during the Holocene shows complex patterns of correlation and anti-correlation at different timescales [74]. Our results suggest that the Wushan Loess formation was primarily controlled by strengthened winter monsoon circulation during glacial periods, with enhanced dust transport from northwestern sources [72,75–77].

Recent studies on the impact of Tibetan Plateau warming amplification on interannual variations in East Asian summer precipitation demonstrate the continuing influence of this major topographic feature on regional climate patterns [78]. The long-term effects of the Tibetan Plateau have contributed to intensified aridity in inland Asia through complex feedback mechanisms, including dust-ice cloud interactions [79]. These processes have facilitated the expansion of dust source regions and enhanced aeolian transport to southern China during the Late Pleistocene.

The Wushan Loess, as an important aeolian sedimentary record in the Yangtze Three Gorges region, not only reflects the influence of regional geological processes on loess formation but also records critical information about Late Pleistocene East Asian monsoon systems and atmospheric circulation patterns [80,81]. This provides new evidence and perspectives for understanding relationships among climate, tectonics, geomorphology, and dust accumulation in the Yangtze River basin. Future work could benefit from mineral composition analysis of the silt fraction and stable isotope measurements ($\delta^{13}C$, $\delta^{18}O$) on carbonate nodules to further constrain paleoenvironmental conditions and sediment diagenesis [82–86].

6. Conclusions

Through comprehensive analysis employing detrital zircon U-Pb geochronology, OSL chronology, and detailed grain size analysis of Late Pleistocene Wushan Loess, combined with comparisons to sediments from the upper Yangtze River basin and northern China, the following conclusions can be drawn:

(1) Chronological Framework and Depositional Continuity

OSL dating establishes a robust chronological framework spanning 18.1 ± 1.20 ka to 103.8 ± 5.11 ka (MIS 2 to MIS 5), demonstrating continuous loess deposition during the Late Pleistocene glacial period. Mean sedimentation rates range from 9.27 to 14.58 cm/ka across the three profiles, consistent with enhanced East Asian winter monsoon activity during this interval. The chronology provides critical temporal constraints for understanding dust accumulation patterns in southern China.

(2) Aeolian Origin and Transport Mechanisms

Grain size analysis reveals dominant silt fractions (72%–78%) with modal sizes of 20–25 μm, characteristic of aeolian transport. The bimodal grain size distributions, combined with C-M diagram analysis and the absence of fluvial sedimentary structures, confirm the wind-blown origin of the Wushan Loess. Fine particles (<20 μm, in all profile>40%) indicate long-distance transport capabilities, while coarse silt (20–63 μm, 45%–52%) suggests significant proximal contributions.

(3) Mixed Provenance Model with Proximal Dominance

Detrital zircon U-Pb age spectra from 1189 analyses reveal consistent major peaks at 200–220 Ma, 450–500 Ma, 720–780 Ma, and 1800–1850 Ma across all profiles. Multi-

dimensional scaling and non-negative least squares unmixing analyses establish a mixed provenance model: approximately 60%–70% proximal contributions from the upper Yangtze River basin and Three Gorges region, and 20%–30% distal contributions from the Loess Plateau and northern Chinese deserts. This represents the first quantitative demonstration of proximal-dominated provenance for the Wushan Loess.

(4) Paleoclimatic and Paleoenvironmental Implications

The formation of Wushan Loess reflects enhanced aridity and strengthened winter monsoon circulation during Late Pleistocene glacial periods. The mixed provenance signatures indicate complex dust transport pathways involving both local valley winds and long-distance atmospheric circulation. The study provides new insights into the southern extent of Chinese loess distribution and its relationship to East Asian monsoon evolution, contributing to our understanding of dust dynamics in monsoon boundary zones.

This study establishes the Wushan Loess as a valuable paleoclimatic archive recording Late Pleistocene atmospheric circulation changes in southern China. The methodological integration of large-n detrital zircon datasets (with ~420 grains measured per profile) with multi-proxy analysis provides a robust framework for future provenance studies of southern Chinese aeolian deposits. The results have important implications for understanding climate–tectonic interactions and dust transport mechanisms in the context of East Asian monsoon system evolution.

Supplementary Materials: The following supporting information can be downloaded at https://www.mdpi.com/article/10.3390/min15111180/s1, Table S1: Wushan Loess and its potential source areas Detrital zircon U-Pb geochronological data and sources; Method Description: Multidimensional Scaling (MDS) Analysis.

Author Contributions: Conceptualization, X.H. and C.L.; methodology, Y.Z.; software, X.H.; validation, G.L. and M.J.; formal analysis, Y.L.; investigation, Y.Z. and J.S.; resources, C.L. and Y.L.; data curation, X.H.; writing—original draft preparation, X.H. and J.L.; writing—review and editing, Y.Z.; visualization, G.L.; supervision, X.H.; project administration, C.L.; funding acquisition, C.L. All authors have read and agreed to the published version of the manuscript.

Funding: This research was funded by the National Natural Science Foundation of China (Grant No. 41871019, 41672355, 41877292 and 41671011), provincial projects of Hubei: "Wuhan Multi-factor Urban Geological Survey Demonstration Project" (Grant No. WHDYS-2018-007) and the "Provenance and Environment of Wushan Loess Research Program" of the China University of Geosciences (Grant No. 106kz18w30203).

Data Availability Statement: The data presented in this study are available from the corresponding authors upon reasonable request. We welcome collaboration and will track data usage to foster future joint publications.

Acknowledgments: We would like to express our special gratitude to Xu Lin from China Three Gorges University for his experimental advice, paper writing guidance, and data support in this study. During the preparation of this manuscript/study, the authors used AI language tools for the purposes of English translation and grammar check. The authors have reviewed and edited the output and take full responsibility for the content of this publication."

Conflicts of Interest: Jianchao Su is an employee of Yellow River Engineering Consulting Co., Ltd. The paper reflects the views of the scientists and not the company.

Abbreviations

The following abbreviations are used in this manuscript:

OSL	optically stimulated luminescence
MIS	Marine Isotope Stage
U-Pb	Uranium–Lead
Th/U	Thorium/Uranium
KDE	Kernel Density Estimation
MDS	Multi-Dimensional Scaling
NNLS	Non-negative Least Squares
ICP-MS	Inductively Coupled Plasma Mass Spectrometry
LA-ICP-MS	Laser Ablation–Inductively Coupled Plasma Mass Spectrometry
SEM	Scanning Electron Microscopy
CL	Cathodoluminescence
TGY	Three Gorges-Yangtze
SCB	Sichuan Basin
WLP	Western Loess Plateau
MUD	Mu Us Desert
QB	Qaidam Basin
SPG	Songpan-Ganzi
TGD	Tengger Desert

References

1. Liu, T.S. *Loess and the Environment*; China Ocean Press: Beijing, China, 1985.
2. Guo, Z.T.; Ruddiman, W.F.; Hao, Q.Z.; Wu, H.B.; Qiao, Y.S.; Zhu, R.X.; Peng, S.Z.; Wei, J.J.; Yuan, B.Y.; Liu, T.S. Onset of Asian desertification by 22 Myr ago inferred from loess deposits in China. *Nature* **2002**, *416*, 159–163. [CrossRef] [PubMed]
3. Sun, J.; Ding, Z.; Liu, T.; Rokosh, D.; Rutter, N. 580,000-year environmental reconstruction from aeolian deposits at the Mu Us Desert margin, China. *Quat. Sci. Rev.* **1999**, *19*, 1351–1364. [CrossRef]
4. Nie, J.; Pullen, A.; Garzione, C.N.; Peng, W.; Wang, Z. Pre-Quaternary decoupling between Asian aridification and high dust accumulation rates. *Sci. Adv.* **2018**, *4*, eaao6977. [CrossRef] [PubMed]
5. Pye, K.; Zhou, L.P. Late Pleistocene and Holocene aeolian dust deposition in North China and the Northwest Pacific Ocean. *Palaeogeogr. Palaeoclimatol. Palaeoecol.* **1989**, *73*, 11–23. [CrossRef]
6. Ding, Z.L.; Yu, Z.W.; Rutter, N.W.; Liu, T.S. Towards an orbital time scale for Chinese loess deposits. *Quat. Sci. Rev.* **1994**, *13*, 39–70. [CrossRef]
7. Mejdahl, V.; Bøtter-Jensen, L. Luminescence dating of archaeological materials using a new technique based on single aliquot measurements. *Quat. Sci. Rev.* **1994**, *13*, 551–554. [CrossRef]
8. Prescott, J.R.; Hutton, J.T. Cosmic ray contributions to dose rates for luminescence and ESR dating: Large depths and long-term time variations. *Radiat. Meas.* **1994**, *23*, 497–500. [CrossRef]
9. Porter, S.C.; An, Z. Correlation between climate events in the North Atlantic and China during the last glaciation. *Nature* **1995**, *375*, 305–308. [CrossRef]
10. Stevens, T.; Carter, A.; Watson, T.P.; Vermeesch, P.; Andò, S.; Bird, A.F.; Lu, H.; Garzanti, E.; Cottam, M.A.; Sevastjanova, I. Genetic linkage between the Yellow River, the Mu Us desert and the Chinese Loess Plateau. *Quat. Sci. Rev.* **2013**, *78*, 355–368. [CrossRef]
11. Wiedenbeck, M.; Allé, P.; Corfu, F.; Griffin, W.L.; Meier, M.; Oberli, F.; Von Quadt, A.; Roddick, J.C.; Spiegel, W. Three natural zircon standards for U-Th-Pb, Lu-Hf, trace element and REE analyses. *Geostand. Newsl.* **1995**, *19*, 1–23. [CrossRef]
12. Xiao, J.; Porter, S.C.; An, Z.; Kumai, H.; Yoshikawa, S. Grain size of quartz as an indicator of winter monsoon strength on the Loess Plateau of central China during the last 130,000 yr. *Quat. Res.* **1995**, *43*, 22–29. [CrossRef]
13. Weltje, G.J. End-member modeling of compositional data: Numerical-statistical algorithms for solving the explicit mixing problem. *Math. Geol.* **1997**, *29*, 503–549. [CrossRef]
14. Aitken, M.J. *An Introduction to Optical Dating*; Oxford University Press: Oxford, UK, 1998.
15. Rea, D.K.; Snoeckx, H.; Joseph, L.H. Late Cenozoic eolian deposition in the North Pacific: Asian drying, Tibetan uplift, and cooling of the northern hemisphere. *Paleoceanography* **1998**, *13*, 215–224. [CrossRef]
16. Galbraith, R.F.; Roberts, R.G.; Laslett, G.M.; Yoshida, H.; Olley, J.M. Optical dating of single and multiple grains of quartz from Jinmium rock shelter, northern Australia: Part I, experimental design and statistical models. *Archaeometry* **1999**, *41*, 339–364. [CrossRef]

17. Petit, J.R.; Jouzel, J.; Raynaud, D.; Barkov, N.I.; Barnola, J.M.; Basile, I.; Bender, M.; Chappellaz, J.; Davis, M.; Delaygue, G. Climate and atmospheric history of the past 420,000 years from the Vostok ice core, Antarctica. *Nature* **1999**, *399*, 429–436. [CrossRef]
18. Murray, A.S.; Wintle, A.G. Luminescence dating of quartz using an improved single-aliquot regenerative-dose protocol. *Radiat. Meas.* **2000**, *32*, 57–73. [CrossRef]
19. An, Z.; Kutzbach, J.E.; Prell, W.L.; Porter, S.C. Evolution of Asian monsoons and phased uplift of the Himalaya-Tibetan Plateau since Late Miocene times. *Nature* **2001**, *411*, 62–66. [CrossRef]
20. Ding, Z.L.; Sun, J.M.; Yang, S.L.; Liu, T.S. Geochemistry of the Pliocene red clay formation in the Chinese Loess Plateau and implications for its origin, source provenance and paleoclimate change. *Geochim. Cosmochim. Acta* **2001**, *65*, 901–913. [CrossRef]
21. Porter, S.C. Chinese loess record of monsoon climate during the last glacial-interglacial cycle. *Earth Sci. Rev.* **2001**, *54*, 115–128. [CrossRef]
22. Wang, Y.J.; Cheng, H.; Edwards, R.L.; An, Z.S.; Wu, J.Y.; Shen, C.C.; Dorale, J.A. A high-resolution absolute-dated late Pleistocene monsoon record from Hulu Cave, China. *Science* **2001**, *294*, 2345–2348. [CrossRef]
23. Andersen, T. Correction of common lead in U-Pb analyses that do not report 204Pb. *Chem. Geol.* **2002**, *192*, 59–79. [CrossRef]
24. Ding, Z.L.; Derbyshire, E.; Yang, S.L.; Yu, Z.W.; Xiong, S.F.; Liu, T.S. Stacked 2.6-Ma grain size record from the Chinese loess based on five sections and correlation with the deep-sea δ18O record. *Paleoceanography* **2002**, *17*, 1033. [CrossRef]
25. Sun, D.; Bloemendal, J.; Rea, D.K.; Vandenberghe, J.; Jiang, F.; An, Z.; Su, R. Grain-size distribution function of polymodal sediments in hydraulic and aeolian environments, and numerical partitioning of the sedimentary components. *Sediment. Geol.* **2002**, *152*, 263–277. [CrossRef]
26. Bøtter-Jensen, L.; Andersen, C.E.; Duller, G.A.T.; Murray, A.S. Developments in radiation, stimulation and observation facilities in luminescence measurements. *Radiat. Meas.* **2003**, *37*, 535–541. [CrossRef]
27. Corfu, F.; Hanchar, J.M.; Hoskin, P.W.O.; Kinny, P. Atlas of zircon textures. *Rev. Mineral. Geochem.* **2003**, *53*, 469–500. [CrossRef]
28. Duller, G.A.T. Distinguishing quartz and feldspar in single grain luminescence measurements. *Radiat. Meas.* **2003**, *37*, 161–165. [CrossRef]
29. Murray, A.S.; Wintle, A.G. The single aliquot regenerative dose protocol: Potential for improvements in reliability. *Radiat. Meas.* **2003**, *37*, 377–381. [CrossRef]
30. Zhang, X.Y.; Gong, S.L.; Zhao, T.L.; Arimoto, R.; Wang, Y.Q.; Zhou, Z.J. Sources of Asian dust and role of climate change versus desertification in Asian dust emission. *Geophys. Res. Lett.* **2003**, *30*, 2272. [CrossRef]
31. Jackson, S.E.; Pearson, N.J.; Griffin, W.L.; Belousova, E.A. The application of laser ablation-inductively coupled plasma-mass spectrometry to in situ U-Pb zircon geochronology. *Chem. Geol.* **2004**, *211*, 47–69. [CrossRef]
32. Lu, H.; Zhang, F.; Liu, X.; Duce, R.A. Periodicities of palaeoclimatic variations recorded by loess-paleosol sequences in China. *Quat. Sci. Rev.* **2004**, *23*, 1891–1900. [CrossRef]
33. Vermeesch, P. How many grains are needed for a provenance study? *Earth Planet. Sci. Lett.* **2004**, *224*, 441–451. [CrossRef]
34. Andersen, T. Detrital zircons as tracers of sedimentary provenance: Limiting conditions from statistics and numerical simulation. *Chem. Geol.* **2005**, *216*, 249–270. [CrossRef]
35. Borg, I.; Groenen, P.J.F. *Modern Multidimensional Scaling: Theory and Applications*, 2nd ed.; Springer: New York, NY, USA, 2005.
36. Ding, Z.L.; Derbyshire, E.; Yang, S.L.; Sun, J.M.; Liu, T.S. Stepwise expansion of desert environment across northern China in the past 3.5 Ma and implications for monsoon evolution. *Earth Planet. Sci. Lett.* **2005**, *237*, 45–55. [CrossRef]
37. Fang, X.; Yan, M.; Van der Voo, R.; Rea, D.K.; Song, C.; Parés, J.M.; Gao, J.; Nie, J.; Dai, S. Late Cenozoic deformation and uplift of the NE Tibetan Plateau: Evidence from high-resolution magnetostratigraphy of the Guide Basin, Qinghai Province, China. *Geol. Soc. Am. Bull.* **2005**, *117*, 1208–1225. [CrossRef]
38. Zhao, H.; Li, S.H. Internal dose rate to K-feldspar grains from radioactive elements other than potassium. *Radiat. Meas.* **2005**, *40*, 84–93. [CrossRef]
39. Qiao, Y.; Guo, Z.; Hao, Q.; Yin, Q.; Yuan, B.; Liu, T. Grain-size features of a Miocene loess-soil sequence at Qinan: Implications on its origin. *Sci. China Ser. D Earth Sci.* **2006**, *49*, 731–738. [CrossRef]
40. Sun, J.; Liu, T. The age of the Taklimakan Desert. *Science* **2006**, *312*, 1621. [CrossRef]
41. Sun, Y.; Chen, J.; Clemens, S.C.; Liu, Q.; Ji, J.; Tada, R. East Asian monsoon variability over the last seven glacial cycles recorded by a loess sequence from the northwestern Chinese Loess Plateau. *Geochem. Geophys. Geosyst.* **2006**, *7*, Q12Q02. [CrossRef]
42. Sun, Y.; Clemens, S.C.; An, Z.; Yu, Z. Astronomical timescale and palaeoclimatic implication of stacked 3.6-Myr monsoon records from the Chinese Loess Plateau. *Quat. Sci. Rev.* **2006**, *25*, 33–48. [CrossRef]
43. Wintle, A.G.; Murray, A.S. A review of quartz optically stimulated luminescence characteristics and their relevance in single-aliquot regeneration dating protocols. *Radiat. Meas.* **2006**, *41*, 369–391. [CrossRef]
44. Roberts, H.M. Assessing the effectiveness of the double-SAR protocol in isolating a luminescence signal dominated by quartz. *Radiat. Meas.* **2007**, *42*, 1627–1636. [CrossRef]
45. Liu, Y.; Hu, Z.; Gao, S.; Günther, D.; Xu, J.; Gao, C.; Chen, H. In situ analysis of major and trace elements of anhydrous minerals by LA-ICP-MS without applying an internal standard. *Chem. Geol.* **2008**, *257*, 34–43. [CrossRef]

46. Richardson, N.J.; Densmore, A.L.; Seward, D.; Fowler, A.; Wipf, M.; Ellis, M.A.; Li, Y.; Zhang, Y. Extraordinary denudation in the Sichuan Basin: Insights from low-temperature thermochronology adjacent to the eastern margin of the Tibetan Plateau. *J. Geophys. Res. Solid Earth* **2008**, *113*, B04409. [CrossRef]
47. Sláma, J.; Košler, J.; Condon, D.J.; Crowley, J.L.; Gerdes, A.; Hanchar, J.M.; Horstwood, M.S.A.; Morris, G.A.; Nasdala, L.; Norberg, N. Plešovice zircon—A new natural reference material for U-Pb and Hf isotopic microanalysis. *Chem. Geol.* **2008**, *249*, 1–35. [CrossRef]
48. Thomsen, K.J.; Murray, A.S.; Jain, M.; Bøtter-Jensen, L. Laboratory fading rates of various luminescence signals from feldspar-rich sediment extracts. *Radiat. Meas.* **2008**, *43*, 1474–1486. [CrossRef]
49. Yang, S.; Ding, Z. Advance-retreat history of the East-Asian summer monsoon rainfall belt over northern China during the last two glacial-interglacial cycles. *Earth Planet. Sci. Lett.* **2008**, *274*, 499–510. [CrossRef]
50. Yang, X.; Zhu, B.; Wang, X.; Li, C.; Zhou, Z.; Chen, J.; Yin, J.; Lu, Y. Late Quaternary environmental changes and organic carbon density in the Hunshandake Sandy Land, eastern Inner Mongolia, China. *Glob. Planet. Change* **2008**, *61*, 70–78. [CrossRef]
51. Zhang, Y.; Li, C.; Yan, L.; Hu, S.; Cheng, X. Magnetic Fabric of Aqueous and Aeolian Sediments in the Middle Yangtze River. *Acta Geol. Sin.* **2008**, *82*, 857–863.
52. Guo, Z.T.; Berger, A.; Yin, Q.Z.; Qin, L. Strong asymmetry of hemispheric climates during MIS-13 inferred from correlating China loess and Antarctica ice records. *Clim. Past* **2009**, *5*, 21–31. [CrossRef]
53. Liang, M.; Guo, Z.; Kahmann, A.J.; Oldknow, C. Geochemical characteristics of the Miocene eolian deposits in China: Their provenance and climate implications. *Geochem. Geophys. Geosyst.* **2009**, *10*, Q04004. [CrossRef]
54. Liu, Z.; Otto-Bliesner, B.L.; He, F.; Brady, E.C.; Tomas, R.; Clark, P.U.; Carlson, A.E.; Lynch-Stieglitz, J.; Curry, W.; Brook, E. Transient simulation of last deglaciation with a new mechanism for Bølling-Allerød warming. *Science* **2009**, *325*, 310–314. [CrossRef]
55. Pye, K.; Tsoar, H. *Aeolian Sand and Sand Dunes*; Springer: Berlin/Heidelberg, Germany, 2009.
56. Smalley, I.; O'Hara-Dhand, K.; Wint, J.; Machalett, B.; Jary, Z.; Jefferson, I. Rivers and loess: The significance of long river transportation in the complex event-sequence approach to loess deposit formation. *Quat. Int.* **2009**, *198*, 7–18. [CrossRef]
57. Zhang, Y.; Li, C.; Chen, L.; Kang, C.; Hu, S.; Huo, J.; Yan, L.; Cheng, X. Magnetic Fabric Characteristics of the Sandy Sediments in the Middle Reaches of the Yangtze River and Their Indicative Significance of Palaeowind Field. *Acta Geophys. Sin.* **2009**, *52*, 150–156.
58. Clemens, S.C.; Prell, W.L.; Sun, Y. Orbital-scale timing and mechanisms driving Late Pleistocene Indo-Asian summer monsoons: Reinterpreting cave speleothem $\delta^{18}O$. *Paleoceanography* **2010**, *25*, PA4207. [CrossRef]
59. Sun, Y.; An, Z.; Clemens, S.C.; Bloemendal, J.; Vandenberghe, J. Seven million years of wind and precipitation variability on the Chinese Loess Plateau. *Earth Planet. Sci. Lett.* **2010**, *297*, 525–535. [CrossRef]
60. Vermeesch, P.; Fenton, C.R.; Kober, F.; Wiggs, G.F.S.; Bristow, C.S.; Xu, S. Sand residence times of one million years in the Namib Sand Sea from cosmogenic nuclides. *Nat. Geosci.* **2010**, *3*, 862–865. [CrossRef]
61. Wang, Y.; Zhang, A.; Fan, W.; Zhang, F.; Zhang, Y. Petrogenesis of late Triassic post-collisional basaltic rocks of the Lancangjiang tectonic zone, southwest China, and tectonic implications for the evolution of the eastern Paleotethys. *Lithos* **2010**, *120*, 529–546. [CrossRef]
62. Xiong, S.; Ding, Z.; Zhu, Y.; Zhou, R.; Lu, H. A ~6 Ma chemical weathering history, the grain size dependence of chemical weathering intensity, and its implications for provenance change of the Chinese loess–red clay deposit. *Quat. Sci. Rev.* **2010**, *29*, 1911–1922. [CrossRef]
63. Nagashima, K.; Tada, R.; Tani, A.; Sun, Y.; Isozaki, Y.; Toyoda, S.; Hasegawa, H. Millennial-scale oscillations of the westerly jet path during the last glacial period. *J. Asian Earth Sci.* **2011**, *40*, 1214–1220. [CrossRef]
64. Hao, Q.; Wang, L.; Oldfield, F.; Peng, S.; Qin, L.; Song, Y.; Xu, B.; Qiao, Y.; Bloemendal, J.; Guo, Z. Delayed build-up of Arctic ice sheets during 400,000-year minima in insolation variability. *Nature* **2012**, *490*, 393–396. [CrossRef]
65. Wang, E.; Kirby, E.; Furlong, K.P.; van Soest, M.; Xu, G.; Shi, X.; Kamp, P.J.J.; Hodges, K.V. Two-phase growth of high topography in eastern Tibet during the Cenozoic. *Nat. Geosci.* **2012**, *5*, 640–645. [CrossRef]
66. Wang, X.; Lu, H.; Vandenberghe, J.; Zheng, S.; van Balen, R. Late Miocene uplift of the NE Tibetan Plateau inferred from basin filling, planation and fluvial terraces in the Huang Shui catchment. *Glob. Planet. Change* **2012**, *88*, 10–19. [CrossRef]
67. Pye, K. The nature, origin and accumulation of loess. *Quat. Sci. Rev.* **1995**, *14*, 653–667. [CrossRef]
68. Vandenberghe, J. Grain size of fine-grained windblown sediment: A powerful proxy for process identification. *Earth Sci. Rev.* **2013**, *121*, 18–30. [CrossRef]
69. Vermeesch, P. Multi-sample comparison of detrital age distributions. *Chem. Geol.* **2013**, *341*, 140–146. [CrossRef]
70. Gehrels, G. Detrital zircon U-Pb geochronology applied to tectonics. *Annu. Rev. Earth Planet. Sci.* **2014**, *42*, 127–149. [CrossRef]
71. Bird, A.; Stevens, T.; Rittner, M.; Vermeesch, P.; Carter, A.; Andò, S.; Garzanti, E.; Lu, H.; Nie, J.; Zeng, L. Quaternary dust source variation across the Chinese Loess Plateau. *Palaeogeogr. Palaeoclimatol. Palaeoecol.* **2015**, *435*, 254–264. [CrossRef]

72. Nie, J.; Stevens, T.; Rittner, M.; Stockli, D.; Garzanti, E.; Limonta, M.; Bird, A.; Andò, S.; Vermeesch, P.; Saylor, J. Loess Plateau storage of Northeastern Tibetan Plateau-derived Yellow River sediment. *Nat. Commun.* **2015**, *6*, 8511. [CrossRef]
73. Vermeesch, P.; Garzanti, E. Making geological sense of 'Big Data' in sedimentary provenance analysis. *Chem. Geol.* **2015**, *409*, 20–27. [CrossRef]
74. Malusà, M.G.; Resentini, A.; Garzanti, E. Hydraulic sorting and mineral fertility bias in detrital geochronology. *Gondwana Res.* **2016**, *31*, 1–19. [CrossRef]
75. Shao, J.; Tang, L.; Li, Y.; Zhou, Z.; Li, C. Provenance and tectonic-paleogeographic evolution: Constraints from detrital zircon U-Pb ages of Late Triassic-Early Jurassic deposits in the northern Sichuan basin, central China. *J. Asian Earth Sci.* **2016**, *127*, 12–31. [CrossRef]
76. Vermeesch, P.; Resentini, A.; Garzanti, E. An R package for statistical provenance analysis. *Sediment. Geol.* **2016**, *336*, 14–25. [CrossRef]
77. Li, Y.; Song, Y.; Fitzsimmons, K.E.; Chang, H.; Orozbaev, R.; Li, X. Eolian dust dispersal patterns since the last glacial period in eastern Central Asia: Insights from a loess-paleosol sequence in the Ili Basin. *Clim. Past* **2018**, *14*, 271–286. [CrossRef]
78. Yang, M.; Chang, H.; Qin, X.; Burr, G.S.; Liu, W. Aridification in the Asian Interior Recorded by Mineral Assemblages in Tarim Basin since the Late Miocene and Its Link to Global Cooling. *Minerals* **2022**, *12*, 1543. [CrossRef]
79. Lin, X.; Jolivet, M.; Cheng, F. Spatiotemporal Evolution of Central Qilian Shan (Northwest China) Constrained by Fission-Track Ages of Detrital Grains from the Huangshui River. *Minerals* **2023**, *13*, 890. [CrossRef]
80. Lin, X.; Liu-Zeng, J.; Wu, L.; Cleber, S.J.; Liu, D.; Dai, J.; Hu, C.; Chen, X.; Li, L.; Zhang, L. Meso–Cenozoic Exhumation in the South Qinling Shan (Central China) Recorded by Detrital Apatite Fission-Track Dating of Modern River Sediments. *Minerals* **2023**, *13*, 1314. [CrossRef]
81. Lin, X.; Hu, C.; Wu, R.; Qin, L.; Xiang, R.; An, Z.; Lu, H. How Was the Late Neogene Red Clay Formed in the Ordos Plateau (Northwest China)? *Minerals* **2024**, *14*, 537. [CrossRef]
82. Tian, S.; Guan, K.; Lin, X.; Liu, H.; Zhang, Y. The Geochemical Characteristics of Zircon and K-Feldspar Grains from the Lower Yellow and Yangtze Rivers: Implications for Provenance Tracing Studies in the Western Pacific Ocean. *Minerals* **2025**, *15*, 121. [CrossRef]
83. Folk, R.L.; Ward, W.C. Brazos River bar: A study in the significance of grain size parameters. *J. Sediment. Res.* **1957**, *27*, 3–26. [CrossRef]
84. Stacey, J.S.; Kramers, J.D. Approximation of terrestrial lead isotope evolution by a two-stage model. Earth Planet. *Sci. Lett.* **1975**, *26*, 207–221. [CrossRef]
85. Tsoar, H.; Pye, K. Dust transport and the question of desert loess formation. *Sedimentology* **1987**, *34*, 139–153. [CrossRef]
86. Derbyshire, E.; Billard, A.; Van Vliet-Lanoe, B.; Lautridou, J.P.; Cremaschi, M. Loess and palaeoenvironment: Some results of a European joint programme of research. *J. Quat. Sci.* **1988**, *3*, 147–169. [CrossRef]

Disclaimer/Publisher's Note: The statements, opinions and data contained in all publications are solely those of the individual author(s) and contributor(s) and not of MDPI and/or the editor(s). MDPI and/or the editor(s) disclaim responsibility for any injury to people or property resulting from any ideas, methods, instructions or products referred to in the content.